UNIVERSITÀ DEGLI STUDI DI PADOVA

DIPARTIMENTO DI SCIENZE CHIMICHE

CORSO DI LAUREA MAGISTRALE IN SCIENZA DEI MATERIALI

TESI DI LAUREA MAGISTRALE

STM investigation of RuOx submonolayer nanostructures on Pt(111) for alkaline HER

Relatore: Prof. Stefano Agnoli

Controrelatore: Prof. Alessandro Martucci

LAUREANDO: Nalesso Marco

ANNO ACCADEMICO 2021/2022

Sommario

0 Chapter 0: Abstract

Visualizing a model catalyst surface on the atomic scale can help to explain its chemical activity and its properties observed during electrochemical characterization. In this work, carried out in Ultra High Vacuum (UHV) conditions, a Pt(111) single crystal is firstly characterized and then covered with submonolayer films of RuOx deposited via thermally activated chemical vapor deposition (CVD) in presence of an oxygen background pressure. The RuOx/Pt(111) model catalyst, with various coverages obtained by changing deposition time, is initially investigated under UHV via Low-Energy Electron Diffraction (LEED), X-ray Photoelectron Spectroscopy (XPS) and Scanning Tunneling Microscopy (STM). This last technique was abundantly used to understand the deposition process and the growth of the ruthenium film. Afterwards, the sample activity toward the Hydrogen Evolution Reaction (HER) in alkaline conditions is tested in an electrochemical cell to correlate the coverage, composition and morphology of the adlayer to the reaction mechanisms affecting the catalysis, in an effort to understand whether a bifunctional mechanism between platinum and ruthenium is at play during the electrocatalytic evolution of hydrogen.

1 Chapter 1: Introduction

1.1 Introduction

The rates at which environmental disasters occur[1] and the Earth temperature rises[2] are growing faster every year. CO_2 yearly emissions from combustion and industrial processes are continuously increasing, reaching 36.3 Gt in 2021 and showing a worrying trend for the upcoming decades[3]. Overthrowing the current climate trend is not only desirable, but a moral obligation for whoever wishes to survive on this planet. The European summer of 2022 showed to everyone what is waiting for humanity if we don't quickly adjust the trend: aridification, extreme heat, vast wildfires, sudden glaciers' melting and droughts are just some of the plagues that are going to haunt our future like the cruel eagle eternally feasting with Prometheus's liver. If we don't use all of our resources to keep the Earth a habitable place, we will not deserve the epithet of the tormented Prometheus, the "fore-thinker": on the contrary, we will be more similar to his brother Epimetheus, the "afterthinker", the Titan who foolishly accepted Pandora and her box despite Prometheus's warning.

In this context, it is imperative that we strive to develop technologies capable of leading humanity to a more sustainable future. Currently, only 4% of the world's H_2 production comes from

renewable sources[4], mainly due to i) the lower price of fossil fuels from which H_2 can be produced via gas reforming and ii) the high prices of electricity. Electrolysers (see section 1.2) are significant, for they will allow us to store the discontinuous energy produced by renewables into H_2, a clean fuel which, once used (either by combustion or in a fuel cell), only produces water as exhaust gas; on the other hand, it is from water itself, one of the most abundant resources on the planet, that we can split into hydrogen and oxygen via electrolysers, in a virtuous cycle.

Three main technologies are currently being studied for water electrolysis: solid oxide electrolysis (SOEL), proton exchange membrane electrolysis (PEMEL) and alkaline electrolysis (AEL). SOEL requires high temperatures to work properly, between 700 and 900°C, which can be expensive to reach and maintain, and typically operates in very corrosive environments which require the development of appropriate materials[5]. PEMEL is considered a flexible and easy to start up method, but with shorter lifetimes and higher maintenance requirements than AEL[6], which is highly regarded as the most reliable technology for up-scaling H_2 production[7]. For these reasons, we are going to investigate the reaction mechanisms that affect the catalysis of alkaline water electrolysis through model catalysts made of platinum and ruthenium, in an

effort to better understand how to improve the hydrogen production.

Although Pt(111) is among one of the most studied model catalysts, the fields of the unknown still stretch far beyond the horizon over its crystalline planes. Platinum is a noble metal known to be the benchmark catalyst for the acidic hydrogen evolution reaction, which is among the most documented reactions. However, the experimental reaction rate of the same reaction happens to be around two orders of magnitude slower in an alkaline medium. In this case, the nature of the active sites is still unknown, and so is the effect of the pH on the activity. In acidic medium, the hydrogen binding energy serves as a conclusive descriptor of a catalyst activity[8], but it becomes insufficient in an alkaline medium[9]. Within this field lies the design and synthesis of catalysts that may be more efficient and durable than their predecessors. Platinum and ruthenium have already been studied as synergistical and cooperative noble metals for alkaline HER, but very little is still known on the mechanism which allows them to be more active together. While some studies claim that the modulation of platinum electronic structure by ruthenium is the most relevant effect[10], others suggest a bifunctional mechanism through which the more oxyphilic character of ruthenium would easily split water and adsorb OH

groups, letting the platinum sites free to evolve adsorbed hydrogen atoms into molecules[11]. It is currently accepted that the hydrogen adsorption free energy ΔG_{H^*} remains a key thermodynamic descriptor of HER activity, although the overall reaction rate in alkaline medium is strongly affected by the kinetic barrier to water dissociation, while some authors argue that the hydrogen binding energy parameter, conclusive in acidic solutions, is still relevant at pH 13[12].

In this context, a catalyst made of submonolayer nanoislands of RuOx deposited onto a Pt(111) single crystal can be particularly interesting. Given a high interfacial area between the two materials, the activity can be expected to improve significantly if a bifunctional mechanism is at work. Metal oxide phases, due to their lower surface energy, typically expose undercoordinated oxygen atoms which can easily adsorb water and hydroxyl groups, therefore helping platinum to evolve hydrogen at a higher rate. The use of an ultra-high vacuum (UHV) chamber allows to prepare and characterize in a very controlled way the investigated system, while the use of a scanning tunneling microscope (STM) will prove useful in correlating the morphology of the material at the nanometric scale with its catalytic activity precisely and reproducibly.

1.2 Alkaline Electrolysis

1.2.1 Purpose of Alkaline Electrolysis

Electrolysers are devices made of two electrodes, the anode and the cathode, immersed in an electrolytic solution, used to produce hydrogen and oxygen out of water; a schematic view of the system can be seen in Figure 1-1[13].

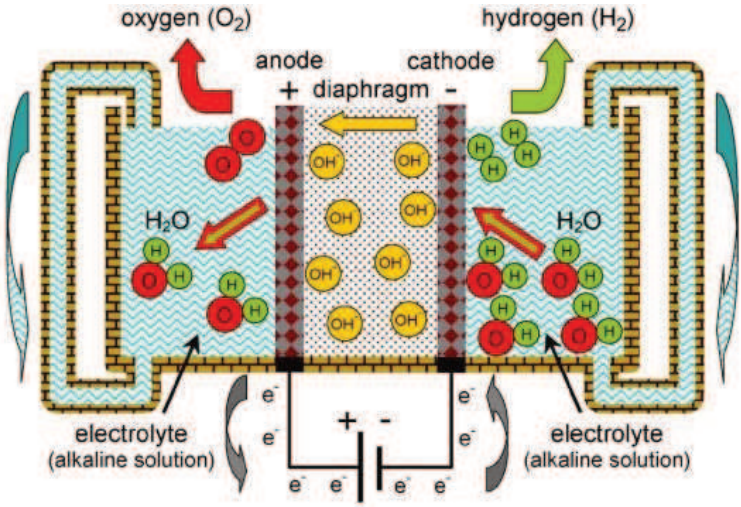

Figure 1-1, schematic representation of an electrolyser.

Alkaline water splitting occurs via two semireactions: the hydrogen evolution reaction (HER) occurs at the cathode, where two water molecules are adsorbed and converted to two hydroxyl ions and hydrogen gas, while at the anode four hydroxyl ions are oxidized into an oxygen molecule and two water molecules, constituting the oxygen evolution reaction (OER)[14]. Given the chance of

the produced gases to react, the two electrodes are usually separated by a diaphragm permeable to the electrolytic solutions but not to gases.

$$Cathode:\ 2H_2O_{(l)} + 2e^- \rightarrow H_{2(g)} + 2OH^-_{(aq)}$$

$$Anode:\ 2OH^-_{(aq)} \rightarrow H_2O_{(l)} + 2e^- + \frac{1}{2}O_{2(g)}$$

$$Overall\ reaction: H_2O_{(l)} \rightarrow \frac{1}{2}O_{2(g)} + H_{2(g)}$$

The produced gas moles are proportional to the number of electrons exchanged, as per the Faraday laws. A better catalyst is therefore one that can exchange higher amounts of current, given a certain applied potential. A good catalyst also needs to be durable, cheap, and easy to produce in high amounts. Figure 1-2, taken from a work by Mahmood et al.[15], shows a Volcano plot for HER in alkaline medium for a few metals[15]: given the (questionable, as will later be discussed) metric of the hydrogen binding energy to the metal on the X axis, the various samples are represented on the graph depending on their exchange current i_0.

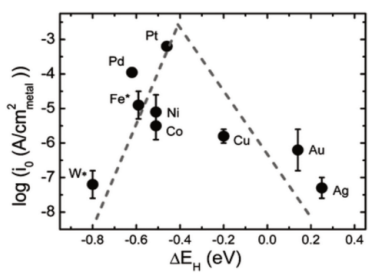

Figure 1-2, Volcano plot representing the activity of various metals for alkaline HER taken from reference 15.

The hydrogen Gibbs free energy of adsorption determines how strongly it interacts with the catalyst surface: if a bond is too weak, hydrogen atoms will be likely to desorb before evolving to the molecular gas, while a bond too strong can prevent diffusion of the atoms on the surface and their further evolution towards the product, *de facto* poisoning the catalyst.

i_0, the exchange current, is a kinetic indicator of how well a reaction performs, fundamental in the Butler-Volmer equation:

$$i = i_0 \left[exp\left(\frac{(1-\alpha)nF\eta}{RT}\right) + exp\left(-\frac{\alpha nF\eta}{RT}\right)\right]$$

When the overpotential η, which is the difference between the applied potential and the equilibrium thermodynamic potential, is equal to zero, then the current is equal to the exchange current. The higher the exchange current, the lower the kinetic barriers to the electron transfer and, therefore, the reaction rate is faster.

Depending on the hydrogen bonding energy to the surface and on other kinetic barriers, three main processes can be the rate determining step to alkaline HER:

i) Volmer reaction: water reduction and adsorption of hydrogen atoms

$$M + H_2O_{(l)} + e^- \rightarrow MH_{ad} + OH^-_{(aq)}$$

ii) Heyrovsky reaction: electrochemical hydrogen desorption

$$MH_{ad} + H_2O_{(l)} + e^- \rightarrow M + H_{2(g)} + OH^-_{(aq)}$$

iii) Tafel reaction: chemical hydrogen desorption

$$2MH_{ad} \rightarrow 2M + H_{2(g)}$$

In absence of H^+ ions in the solution, the Volmer step is deemed necessary, while the other two can occur either simultaneously or exclusively, depending on the conditions. In case of high applied overpotential in a region where the electron transfer is the rate determining step, from the Butler-Volmer equation one can derive the Tafel law.

$$Tafel\ Law\text{:}\ \lim_{\eta\to\infty} i_0 \left[exp\left(\frac{(1-\alpha)nF\eta}{RT}\right) exp\left(-\frac{\alpha nF\eta}{RT}\right)\right] \Longrightarrow \eta$$
$$= \ln|i_0|\frac{RT}{\alpha nF} - \ln|i|\frac{RT}{\alpha nF} = a + b\ln|i|$$

Depending on the catalyst and on the experimental conditions, one can determine a value of the Tafel slope b, an indicator of which of the three aforementioned steps is the rate determining one. In an alkaline medium, the Rate Determining Step (RDS) of HER for the basal plane on a Pt(111) crystal is supposed to be the water dissociation, i.e. the Volmer step which has an associated theoretical Tafel slope of 120 mV/dec, but experimental measurements can lead to multiple possible values between 50 and 150 mV/dec[9,16].

1.2.2 Alkaline HER on Pt(111) and the addition of Ruthenium

The mechanism of the alkaline hydrogen evolution reaction on a Pt(111) crystal is highly debated. Noble metals such as Pt, Pd, Ru and Ir, which strongly interact with hydrogen, can adsorb it at more positive potentials than its evolution equilibrium one. This phenomenon, known as under-potential deposition of hydrogen (H_{upd}), determines the formation of a chemisorbed monolayer of hydrogen prior to its evolution[17]. Even though the alkaline activity is around two orders of magnitude lower than in acidic medium, H_{upd} is the same and metal-hydrogen bond is equally strong in both environments (around 240 kJ/mol)[16]. These experimental results constitute a good argument against a theory according to which

the hydrogen bonding energy (HBE) can be regarded as the main descriptor of activity. In fact, from a thermodynamic point of view, H_{upd} should occur identically in acidic and alkaline environments. The limits to alkaline HER on Pt(111) must therefore be either kinetic, as an extra energy barrier to hydrogen adsorption is required by the extra step of water dissociation necessary at high pH, or related to entropic barriers associated with the crossing of the double layer.

A recent computational study[18], focused on the Pt(111) HER dependence on pH, demonstrated that the adsorption energy of OH^- on Pt(111) is potential-dependent, due to the charged nature of the ion. A more negative field was naturally found to weaken the adsorption. Given the concentration of H^+ ions at pH 13, the authors also considered that the proton donor could either be H_3O^+ or H_2O, calculating that the proton transfer barriers were larger than in acidic media, thus introducing a kinetic barrier. This is consistent with a study by Markovic et al.[19] reporting that, while the heat of adsorption of both H and OH on Pt(111) is essentially independent on pH, at low overpotentials the catalyst surface sites can be occupied by OH_{ad}, blocking the adsorption of H. Interestingly, the higher OH surface coverage was found to be a reason for the

enhanced catalysis of CO oxidation in alkaline medium with respect to an acidic one.

Platinum and ruthenium in catalysis and their interaction

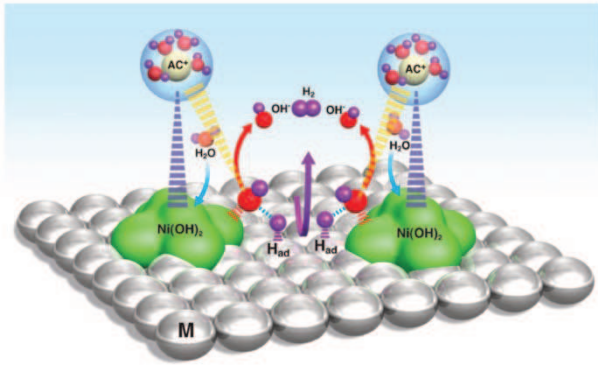

Figure 1-3: Schematic representation of water dissociation, formation of M-Had intermediates, and subsequent recombination of two H_{ad} atoms to form H_2 (magenta arrow) as well as OH^- desorption from the $Ni(OH)_2$ domains (red arrows) followed by adsorption of another water molecule on the same site (blue arrows)[17].

The Volmer step, i.e. the water dissociation, constitutes the main kinetic barrier to alkaline HER, and therefore it is one of the most important aspects that need to be taken into consideration when designing a Pt-based catalyst. Similar reasonings pushed Markovic et al.[20] to make a Pt(111) catalyst onto which $Ni(OH)_2$ nanoislands were deposited. The vast triple phase boundaries between $Pt(111)/Ni(OH)_2/H_2O$, as shown in Figure 1-3, constituted an

efficient system in which the metal oxide could dissociate water and platinum could then evolve the adsorbed hydrogen atoms to molecular hydrogen.

Experiments with similar purposes were performed by Xue et al.[21] through Ni-Fe clusters deposited onto a Pt(111) surface. Ni-hydroxide is known to help the water dissociation step, while platinum is among the best materials for the production of H_2 once hydrogen is adsorbed onto its surface, and Ni-Fe hydroxides were found to be even more active than Ni hydroxides for the OER. Moreover, they investigated the surface morphology via STM, finding a Volmer-Weber growth mechanism appropriate for depositing 3D clusters. All of their samples performed better than pure Pt(111) and the best performing one was found to be that with the most interface area between platinum and the NiFe clusters. The authors suggested that the increased activity may come from a cooperative effect between the two catalytic moieties. On the one hand, the presence of iron in the alloy clusters tunes the OH_{ad} binding energy in comparison to Ni only clusters, helping to dissociate the water. On the contrary, an excessive OH_{ad} binding energy would poison the clusters, as documented in the case of Co doping. On the other hand, platinum would benefit from the improved water dissociation, adsorbing protons to perform HER.

As explained in a previous section, the HBE cannot be a sufficient catalytic descriptor in alkaline pH: in fact, Pt(111) has an almost ideal ΔG_{H^*} both at pH 1 and 13, but at higher pH is limited by the water dissociation step. Similarly to the previous case, in which Ni was known to boost the water dissociation step, the Ru(0001) surface is also known to possess a low water dissociation barrier, while at the same time its negative ΔG_{H^*} inhibits the desorption of the produced hydrogen. UHV studies by Karlberg et al.[10] on various metal surfaces showed that, out of several inspected metal surfaces, Ru(0001) has the strongest interaction with adsorbed H* and OH*, while other spectroscopic experiments in UHV confirmed that water is much more unstable on it than on Pt, a characteristic common to 4d Pt-group metals (Ru, Rh, Pd) when compared to the 5d ones (Pt, Ir)[22]. Interestingly, this same article points out that all Pt-group metals adsorb dissociatively water better with an oxygen coverage below 0.2 ML. By analogy with the previously mentioned Pt(111)/$Ni(OH)_2$ system, it can be therefore easily deduced that by designing a material in which a high interfacial area between Ru, particularly capable of dissociating water and retaining OH, and Pt, which on the other hand has great hydrogen evolution capabilities, could be extremely promising for electrolysis.

For these reasons, bifunctional mechanisms between Pt and Ru have now been proposed for quite some time. Strmcnik et al.[23] suggested that Pt could be improved for HOR by alloying with Ru or other more oxyphilic metals, which would provide sites for OH_{ad}. This was later attempted by Schwammlein et al.[10], who synthesized Ru-core Pt-shell nanoparticles with various degrees of coverage. They proposed that the bifunctional mechanism for HOR could be made of three steps:

(1) $0.5H_2 + Pt \rightarrow Pt - H_{ads}$;

(2) $Ru + OH^- \rightarrow Ru - OH_{ads} + e^-$;

(3) $Pt - H_{ads} + Ru - OH_{ads} \rightarrow Pt + Ru + H_2O$;

however, they also suggested that the bifunctional mechanism would be of minor importance than the electronic modulation effect induced by Ru on Pt which lowers the hydrogen adsorption barrier. However, another study[11] demonstrated that the lower energy Pt-H bond, visible by the H_{upd} shift, can be ascribed to the presence of superficial Ru rather than to an electronic effect, while also asserting that the presence of oxyphilic metals capable of forming oxyhydroxides (such as Ru) would lower the energy barrier for the Volmer step for both HER and HOR, as in the case of the suggested bifunctional mechanism between $Ni(OH)_2$ adislands

over Pt(111)[20]. This hypothesis was also reinforced by a study[24] that, by modifying the platinum surface with various transition metals, proposed that the metal-OH bond strength and its oxophilicity was key to the improved alkaline HER activity and a relevant activity descriptor.

According to a very recent article[25], however, a linear dependency was found between the Ru coverage over Pt and exchange current for HER/HOR, which seems to negate the importance of a bifunctional effect. Instead, the authors suggested that the higher OH binding energy on the more oxyphilic Ru and a shifted H binding energy due to the platinum substrate could influence the activity. From DFT calculations, it was also inferred that the easiest alkaline HER path would be a Volmer-Tafel one, while the Heyrovski step would not be as favourable. These effects, according to the authors, would globally arise from a positive shift of the density of states of the *d* metal orbitals of surface metal atoms from -2.24 eV for clean Pt(111) to -1.10 eV for Ru-covered Pt.

1.3 Utility of UHV in investigation of catalyst properties

UHV studies have often demonstrated to be useful for determining the catalytic properties of metals and other materials even if, at first glance, they may seem too distant from the operative conditions to actually help understand them. An extensive report by Hodgson and Haq[26] shows how UHV techniques like STM, XPS, XAS, vibrational spectroscopies, He scattering and LEED can investigate the modes of adsorption, dissociative or not, of water on metal surfaces. They reported that water does in fact adsorb intact on Pt(111), easily desorbing at 160 K with zero order kinetics, which confirms the difficulties that platinum has to dissociate water molecules. On the other hand, water was found to form intact structures on Ru(0001) only below 155 K, above which a more complex network of OH/H_2O adsorbates exists. Another interesting study by Koper tries to link UHV water dissociation experiments, DFT calculation of H, OH and H_2O binding energies and blank acid cyclovoltammetries for various metals with hexagonal-like surfaces[27]. He suggested that, from the binding energies, one may predict a sort of phase diagram of the adsorbed species on the metal surface and the potentials at which transitions occur.

In absence of an EC-STM study, through which it would be possible to observe directly the catalyst surface and its activity at the same

time[28,29], UHV STM allows to investigate the surface morphology after treatments and depositions, allowing to link the morphology of the adsorbates to the catalytic properties, as many previous studies proved[30–32]. By determining the morphology of adsorbates, which atoms are exposed and undercoordinated and how gases adsorb and react over the prepared surfaces, atomically resolved images can also lay the ground for subsequent DFT works that, by calculating the system energetics, can shed light on reactions mechanisms and the reasons why certain catalyst perform better than others[33–36].

2 Chapter 2: Materials and Characterization Methods

2.1 UHV System

Most of the reported experiments take place within a modified VG-Escalab MkII UHV system, which can be seen in Figure 2-1. It is composed of three main chambers: one, on the right, for LEED analysis and the preparation of samples, i.e. cleaning by cycles of Ar^+ ion bombardment and annealing and also film depositions by

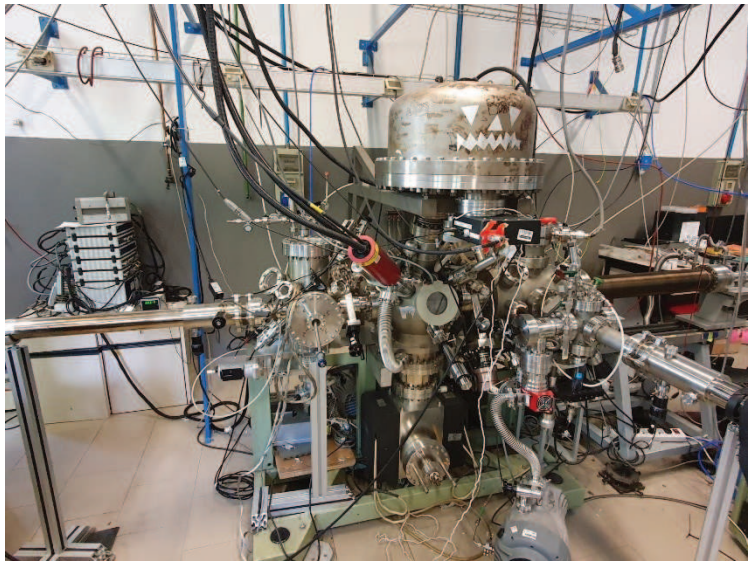

Figure 2-1: picture of the modified VG-Escalab MkII. The STM chamber lies on the left side; in the center there is the analysis chamber, surmounted by the XPS analyser. On the right, the main preparation and LEED chamber (partially hidden) and a fast-entry chamber.

CVD and PVD; one, in the middle, for XPS, UPS and angle-resolved photoemission spectroscopies; and one, on the left, equipped with an STM and two gaslines. The prep chamber is also connected to a fourth, smaller chamber, equipped with a transfer arm for inserting the samples in the vacuum system. A motorized manipulator allows to move and rotate the sample between the prep and the analysis chamber, where a wobble stick can clutch the sample and transfer it to a manually movable manipulator which connects the STM and the analysis chamber. Another wobble stick in the STM chamber moves the sample from the manipulator to its STM slot.

2.2 XPS

X-ray photoelectron spectroscopy is a technique specialized in the identification of the elements that compose a surface. It takes advantage of the photoelectronic effect described by Einstein in 1905[37], according to which the atoms of a sample irradiated with high energy photons can ionize and emit electrons. Assuming that the photoelectron is emitted from the surface of the sample, and that it does not undergo inelastic scattering, its kinetic energy (KE) is given by the difference between the energy of the impinging

photons (*hv*), the energy which bound the electron to the atom (BE) and the work function of the sample in vacuum Φ_S:

$$KE = hv - BE - \Phi_s$$

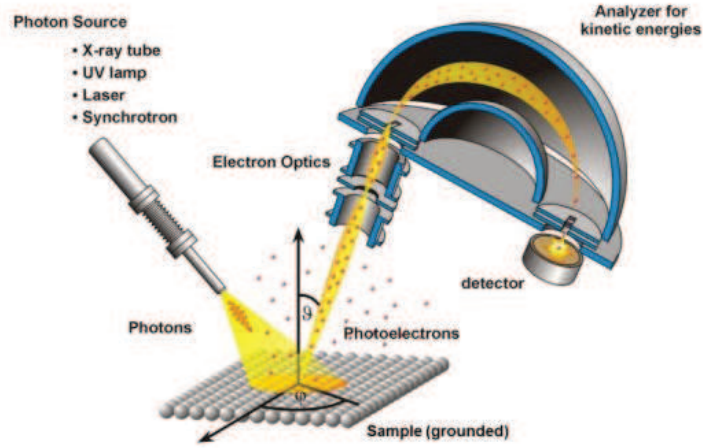

Figure 2-2, scheme of a typical XPS setup[37].

As the schematic image below portrays, an analyzer for kinetic energies is tasked with the collection of the photoelectrons. The analyzer possesses itself a work function Φ_A, which shifts the detected value of KE from its real value:

$$KE = hv - BE - \Phi_s - (\Phi_A - \Phi_s) = \mathrm{hv} - \mathrm{BE} - \Phi_A$$

That considered, the binding energy of the electron photoemitted results:

$$\mathrm{BE} = \mathrm{hv} - \mathrm{KE} - \Phi_A$$

This is a fundamental equation for XPS analysis: given that the photoelectron energy is measured, the photon energy is known and that the work function of the analyzer is empirically found by setting the energy scale to zero at the Fermi edge of reference samples, it is possible to determine the electron binding energies (BE). By comparing the peaks at specific binding energies that emerge from a spectrum with those in literature[38], it is possible to qualitatively identify which elements are present in a sample. The oxidation state of the elements can be determined as well: for example, an oxidized element has a lower electron density than its neutral or reduced counterparts, so the remaining electrons perceive a lower screening of the nuclear positive charges and experience a higher binding energy. The opposite goes for an element in a reduced state, in which electrons have lower binding energies due to a more effective screening. Because of this characteristic, by deconvoluting a photoemission peak it is possible to assess the various chemical states of a given species.

Depending on the atomic orbital considered, the photoemission peak shapes can vary greatly. Electrons from s orbitals give one only peak, whereas electrons form p, d and f orbitals all show a splitting due to spin-orbit coupling. The orbital and spin momentum coupling is described by the quantum number $j = |l \pm s|$,

where l defines the orbital and s the spin. The splitting typically grows with the atomic number and the degeneracy is equal to $2j + 1$. Because of this, given for example a p orbital ($l = 1$), the two observed peaks are named $p_{1/2}$ and $p_{3/2}$ and have a constant area ratio 1:2, whereas for a d orbital ($l = 2$) the peaks are named $d_{3/2}$ and $d_{5/2}$ and have a constant area ratio 2:3. The line shape of a photoemission peak is typically a Lorentzian function, with a natural line width ΔE_0 which depends on the lifetime of the core hole state left by the photoemission process[39]. However, due to temperature-dependent atomic vibrations and instrumental broadening of the peaks, the photoemission peak is better described by a Voigt function, i.e. a convolution of a Gaussian and a Lorentzian curve. In case of electrically conducting materials, the tail at higher binding energy of a peak is longer due to many-body interactions of the photoelectrons with the free ones at the Fermi edge: because of this, a Voigt curve can't describe accurately their peak shapes, and a Doniach-Sunjic line shape is required to account for the asymmetry[39].

Besides the electrons emitted because of the photoelectronic effect by core level and valence bands, Auger peaks can also be found in an XPS spectrum. In fact, after an atom has been ionized, its relaxation process can occur by either X-ray fluorescence or by

Auger electron emission, as shown in Figure 2-3. The former is typical of heavier elements, with atomic number above 35, whereas lighter elements tend to relax via the Auger mechanism. In this case, electrons are emitted with a constant energy that is independent from the X-ray energy: given for example the relaxation of a L1 electron to the K hole with emission of a L2 Auger electron, its kinetic energy is in fact $E_K = (BE_{L1} - BE_K) - BE_{L2}$. Because of this property, Auger lines are found at different binding energies with different X-ray sources, but at the same kinetic energy values.

Another typical characteristic of the XPS spectrum is the inelastic background: as the scanned binding energy grows, so does the background noise. Each peak in fact is not symmetric, for above the average binding energy of the peak the background is significantly higher than below that point. That is because of various loss

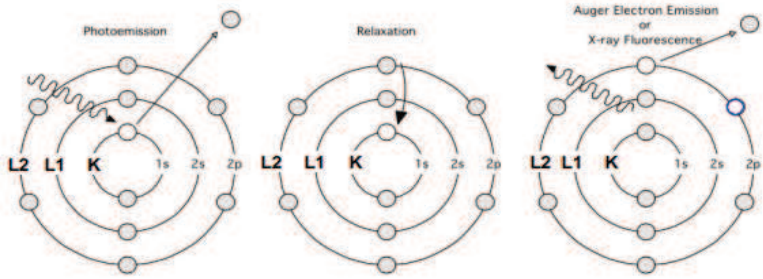

Figure 2-3: schematic resume of the relaxation mechanisms for ionized atoms.

processes determined by the inelastic scattering of electrons. The universal curve of electron inelastic mean free path λ (IMFP), shown in Figure 2-4, represents the average distance electrons can travel within a material between inelastic collisions: at each collision, the electrons lose energy and change their trajectory. It is given by the formula $\lambda(\text{Å}) = E/\{E_p^2[\beta \ln(\gamma E) - (C/E) + (D/E^2]\}$, where E is the photoelectron kinetic energy, $E_p(eV) = 28.821(N_v\rho/M)^{1/2}$ is the free electron plasmon energy, given the bulk density ρ, the number of valence electrons per atom N_v and the atomic molecular mass M, and β, γ, C and D are quantities related to E_p, ρ and the bandgap. Given a photoelectron emitted at depth d, which travels through the material for a d/cosθ length,

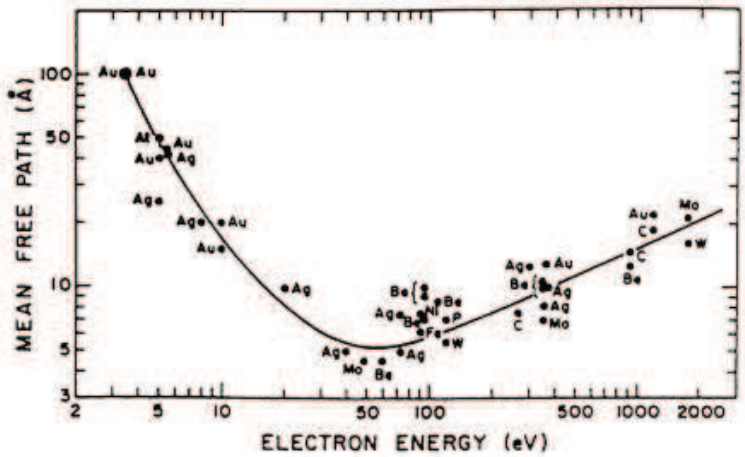

Figure 2-4: "universal" electron mean free path curve[39].

one can calculate the intensity attenuation via the Lambert-Beer equation: $I = I_0 exp\left(\frac{-d}{\lambda cos\theta}\right)$, given I_0, intensity of emitted photoelectrons, and I, the intensity from electrons reaching the surface without energy loss. This equation shows that, for a normal take-off angle, 63% of the electrons emerging unscattered come from within a λ depth, and 86% and 95% of the signal come from respectively a 2λ and 3λ depth[40]. Given that the sampling depth is inversely proportional to $cos\theta$, it is possible to enhance even more the surface sensitivity of XPS by changing the collection angle of the photoelectrons: this is the basis of Angle-Resolved XPS (ARXPS), which can be used for non-destructive depth profiling. The flux of photoelectrons, normalized per unit time and unit energy, emitted from a k level with E_k kinetic energy localized in the infinitesimal volume element dxdydz and moving within the analyser acceptance solid angle $\Omega(E_k, \theta, x, y)$ is given by:

$$dN_k = I_0 exp\left(-\frac{d}{\lambda_e cos\theta}\right) exp\left(-\frac{d}{\lambda_x cos\phi}\right) \cdot \\ \cdot (\rho(d) dx dy dz) D_0(E_k) \left(\frac{d\sigma_k}{d\Omega}\Omega(E_k, \theta, x, y)\right)$$

With $exp\left(-\frac{d}{\lambda_x cos\phi}\right)$ describing the penetration and inelastic attenuation of the x-ray in the sample across the dxdydz volume,

$\rho(d)dxdydz$ the local material density at depth d, and lastly with the differential cross section of photoelectrons being:

$$\frac{d\sigma_k}{d\Omega} = \frac{\sigma_{nl}(E_k)}{4\pi}\left[1 - \frac{1}{2}\beta_{nl}(E_k)\left(\frac{3}{2}cos^2\theta - \frac{1}{2}\right)\right]$$

With $\beta_{nl}(E_k)$ being an asymmetry parameter and $\sigma_{nl}(E_k)$ the total photoemission cross section. As the dN_k equation states, the signal is highly dependent on the emission angle θ. For a given species A, one can consider the relative signal intensity as the contribution of a stack of atomic monolayers, which is given by the general layer by layer equation. For all the monolayers with thickness d_{ML} below the surface,

$$\frac{I_A(\theta)}{I_A^0(\theta)} = \sum_{i=1}^{N} X_A^i \left\{exp\left[-\frac{(i-1)d_{ML}}{\lambda_A cos\theta}\right] - \left[-\frac{id_{ML}}{\lambda_A cos\theta}\right]\right\}$$

Where X_A^i is the mole fraction of the A species in the *i*th layer from the surface. In the simple case of a single layer A on a substrate with composition B (i=1, N=1), by normalizing to an angle θ_0 an equation independent of the mole fractions and of sensitivity factors is obtained:

$$\frac{I_A(\theta)I_B(\theta_0)}{I_B(\theta)I_A(\theta_0)} = \frac{exp\left(\frac{d_A}{\lambda_{A,E(A)}cos\theta}\right) - 1}{exp\left(\frac{d_A}{\lambda_{A,E(A)}cos\theta_0}\right) - 1}$$

This can be used to show how the chemical state shifts between the surface and the bulk and also the assess the stoichiometry of the outermost layers.

In our system, a Mg-kα X-ray source is employed. The sample rotation can be controlled on the polar plane and rotated between the normal orientation and a grazing emission one, at 45°. Survey scans, between 0 and 600-800 eV binding energies, are employed to identify the various elements on the sample, and other high resolution scans are used to obtain more specific information on the oxidation states and area ratios.

2.3 STM

Scanning tunneling microscopy takes advantage of the electron tunneling effect to probe the local density of states of a sample. However, its most important use is probably the direct real-space determination of surface structures in three dimensions. Given a high enough resolution, it allows to observe the surface lattice distances, to measure the height of steps and terraces and even to inspect the density of states below the probe.

The technique, at its most fundamental, uses a sharp metal tip (usually made of tungsten, but sometimes of a platinum-iridium alloy), ideally with a single apex atom extremity, put at just a few Ångstrom above the sample surface, as shown in Figure 2-5. It is moved with atomic scale precision by piezo-electric crystals, in order to scan a square or rectangular area. At this distance, given the application of a bias voltage between the tip and the surface, electrons can overcome the vacuum potential barrier and tunnel from one end to the other, depending on the sign of the bias. Two main modes of operations exist: one at constant height, in which the tip is kept at the same vertical position as it is scanned over the surface, so that the measured current depends on the topography of

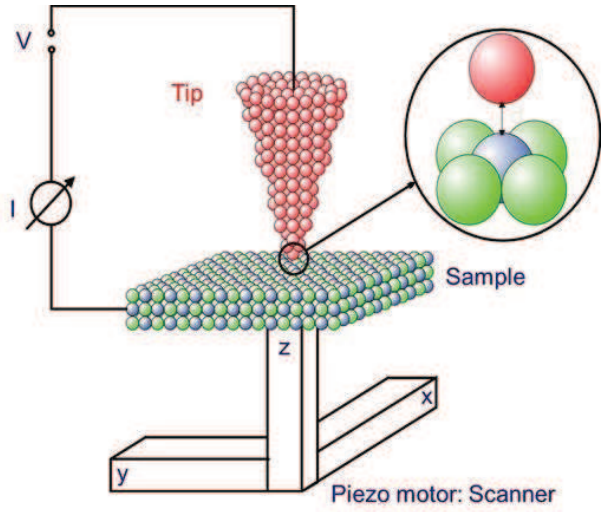

Figure 2-5: minimalistic scheme of how a scanning tunneling microscope[40] works.

the sample, given that it is homogeneous; or a constant current mode, which requires the tip-sample distance to be constant. Such a mode is possible thanks to a feedback system which, given the difference between the set current and the detected current induced by a change of the topography, quickly adjusts the vertical position. This is the scanning mode that will be used in this work, for it allows to distinguish steps, kinks, defects and even to achieve atomic resolution images if the sample and (mostly) tip are of good enough quality. However, this is not often the case.

2.3.1 Tunneling theory

While in classical mechanics a particle in the region x<0 cannot overcome a potential barrier V_0 spanning in the 0<x<d region if it does not possess enough total energy E to surpass it, but is rather reflected or absorbed (in the case of a physical barrier), according to the quantum theory the particle has a small chance to *tunnel* through the barrier, in the region x>d. In this situation, the space of our interest is divided in three regions depending on potential, as shown in Figure 2-6:

$$V_0(x) = \begin{cases} 0, if\ x < 0\ (I) \\ V_0, if\ 0 < x < d\ (II) \\ 0, if\ x > d\ (III) \end{cases}$$

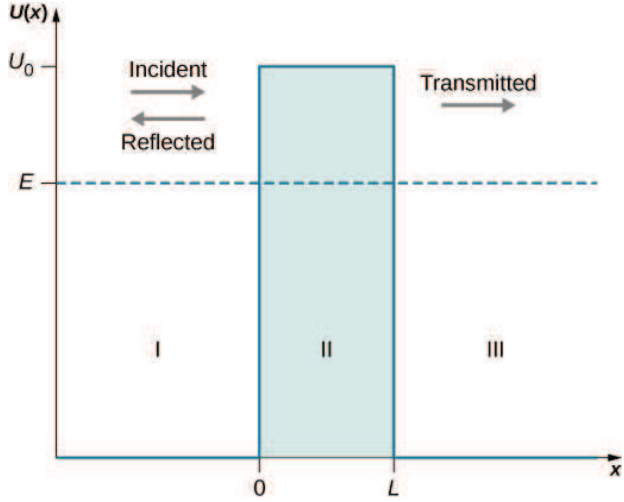

Figure 2-6: schematic representation of the three interesting regions and of the particle's energy E in comparison to the potential barrier V_0[40].

Tunneling is only possible when both V_0 and d are finite: in this case, a part of the particle wave function can penetrate inside the barrier, where it is attenuated, and emerge on the other side.

The particle can be described via the time independent Schrödinger equation:

$$\frac{-\hbar^2}{2m}\frac{d^2\psi(x)}{d^2x} + V(x)\psi(x) = E\psi(x), where -\infty < x < \infty$$

Given the three different areas and $E<V_0$, the wave function of the particle can be described as different sum of exponential functions in the three regions by applying the Wentzel-Kramers Brillouin

approximation, which approximates the electron to a semi-classical particle with a constant wavenumber:

$$(I)\ \psi(x) = Ae^{ik_1 x} + Be^{-ik_1 x} = \psi_{inc}(x) + \psi_{ref}(x)$$

$$(II)\ \psi(x) = Ce^{k_2 x} + De^{-k_2 x}$$

$$(III)\ \psi(x) = Fe^{ik_1 x} + Ge^{-ik_1 x} = \psi_{tra}(x) + 0$$

With $k_1 = \sqrt{\frac{2m_e E}{\hbar}}$ and $k_2 = \sqrt{\frac{2m_e(V_0 - E)}{\hbar}}$ as wavenumbers. In region I, the two waves are respectively incident, moving to the right, and reflected, moving to the left. Since in region III there can only be a transmitted and not a reflected wave, G is set to zero. The probability of transmission, i.e. of tunneling, is defined as the ratio between the transmitted and the incident wave amplitude:

$$T(d, E) = \frac{|\psi_{tra}(x)|^2}{|\psi_{inc}(x)|^2} = \frac{|F|^2}{|A|^2}$$

The equations for adjacent regions are then set as equal at x=0 and x=d, and the same goes for their first order derivatives with respect to x, so to ensure the continuity of solutions at region boundaries. The probability of transmission is therefore:

$$T(d, E) = \frac{1}{cosh^2(\beta d) + (\gamma/2)^2 sinh^2(\beta d)}$$

With $\beta = \sqrt{\frac{2m}{\hbar^2}(V_0 - E)}$ being the attenuation factor of the wave and $(\gamma/2)^2 = \frac{1}{4}\left(\frac{1-E/V_0}{E/V_0} + \frac{E/V_0}{1-E/V_0} - 2\right)$.

In the particular case of quantum tunneling of electrons between a metal surface and an STM tip, according to Bardeen's formalism the current is given by

$$I = \frac{2\pi e}{\hbar}\sum_{\mu,\nu} f(E_\mu)[1 - f(E_\nu + eV)]|M_{\mu\nu}|^2\delta(E_\mu - E_\nu)$$

Where $f(E)$ is the Fermi function, $|M_{\mu\nu}|^2$ is the tunneling matrix element between states of ψ_μ of the probe and ψ_ν of the surface and E_μ is the energy of the state ψ_μ in absence of tunneling.

Tersoff and Hamann[41] developed a comprehensive theory to derive the tunneling current for a probe tip, spherical at the apex and of volume Ω_t as shown in Figure 2-7, by expanding the surface wave function over a **G** series, which is the surface reciprocal-lattice vector. In this way, the matrix element is:

$$M_{\mu\nu} = \frac{\hbar^2}{m} 2\pi\Omega_t^{-1/2} e^{\kappa R} R\psi_\nu(\overrightarrow{r_0})$$

Where $\kappa = \hbar^{-1}(2m\phi)^{1/2}$, $\overrightarrow{r_0}$ is the center of curvature of the tip and R is the radius of the spherical apex of the tip. By substituting, one can find:

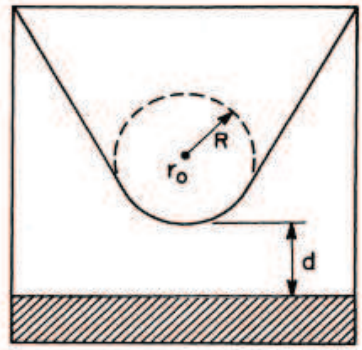

Figure 2-7: schematic view of tunneling geometry. The shape of the tip is considered spherical at the apex, with radius of curvature R, distance d, center of curvature $\overrightarrow{r_0}$ [40].

$$I = \frac{32\pi^3 e^2 V \phi^2 \rho_\nu(E_F) R^2}{\hbar \kappa^4} e^{2\kappa R} \cdot \sum_\nu |\psi_\nu(\overrightarrow{r_0})|^2 \delta(E_\mu - E_\nu)$$

With ρ_ν being the density of states per unit volume of the tip.

An analogous derivation can portray a more digestible current equation:

$$I \propto |\psi_\nu(0)|^2 |\psi_\mu(d)|^2 e^{-2\frac{\sqrt{2m\phi}}{\hbar}d}$$

Which consists of two main parts, one relative to the probability of having electron and empty states available in the probe and the sample, and one depending on the work function ϕ and distance. In the Wentzel-Kramers Brillouin approximation, in fact, by integrating the density of states in a $d\varepsilon$ energy interval, one can find that:

$$T = exp\left(-\frac{2d\sqrt{2m}}{\hbar}\sqrt{\frac{\phi_\mu + \phi_\nu}{2} + \frac{eV}{2} + \varepsilon}\right)$$

$$I \propto \int_0^{eV} \rho_\nu(E_F - eV + \varepsilon)\,\rho_\mu(E_F + \varepsilon)T(\varepsilon, eV)d\varepsilon$$

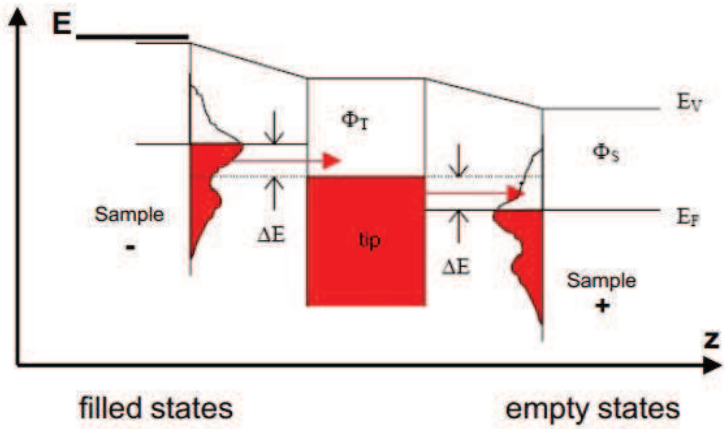

Figure 2-8: scheme representing how changing the bias value and sign dictates which states are being probed.

This shows a strong dependence of the current on the distance but also that, in the constant current mode, the applied bias is a parameter through which one can choose which states are probed. This allows to inspect not only the topography of an area, as the tip distance from the surface changes to keep the current constant, but also the electronic contrast. With a positive bias, the empty states of the sample receive electrons and are inspected, whereas with a negative bias the electrons move from the filled

states of the sample to the tip. In this way it is possible to detect the energy of the surface electrons and where the electron density is higher.

2.3.2 Equipment and methods

A SPM 150 Aarhus microscope by Specs Technologies is used to perform the measurements at room temperature. Tungsten tips inspect the surface and are sputtered the day before or right before STM measurements by a 3.0 keV Ar^+ plasma for 20 minutes. After the tip has been approached with safe tunneling and feedback parameters, the bias is changed between -1 and +1 V and the tunneling current is increased when a flat area is found, in order to attempt to achieve atomic resolution images.

Two leak valves can introduce in the chamber a flow of oxygen, hydrogen of carbon monoxide, depending on what has been loaded for the experiment.

2.4 LEED

Low-Energy Electron Diffraction is a technique which was effectively born and grown in the early 1970s, but conceived already in the 1927 with Davisson and Germer's experiments. As suggested by the name, it employs a beam of low energy electrons, between 20 and 500 eV, i.e. with wavelengths between 0.5 and 2.0 Å according to the De Broglie equation:

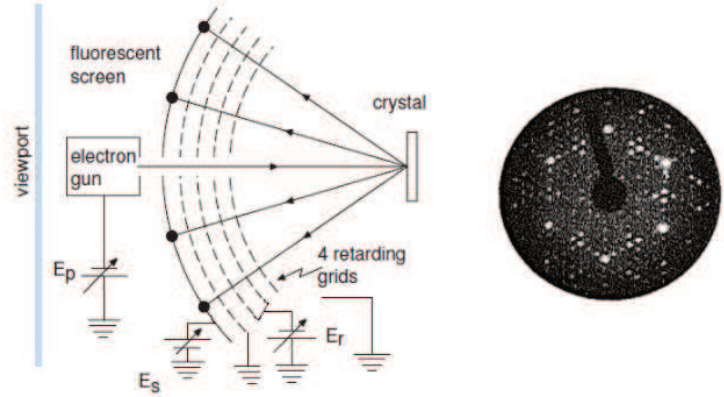

Figure 2-9: a scheme of how a LEED device is made on the left, while a LEED pattern can be seen on the right.

$$\lambda = \frac{h}{\sqrt{2m_e E}} \qquad \lambda_e[nm] \approx \sqrt{\frac{1.5}{E_e\ (eV)}}$$

Electrons guns generate electrons usually via thermoionic effect, by letting a current flow within a filament. A potential difference is then applied to accelerate the electrons towards the sample,

where they can interfere with more or less the outermost 10 Å of the sample, given their low mean escape depths.

If the beam interacts with a crystalline lattice with atomic distances comparable with the electron wavelength, it can scatter coherently: the electrons will then impact on a phosphorescent screen, showing diffraction spots corresponding to the reciprocal lattice points. An advantage of LEED over X-ray diffraction, which studies the crystal structure of powders, polycrystals and single crystals, whereas LEED can only study the surface of single crystals, lies in the ease of modification of the electron energy and therefore their wavelength, a degree of freedom mostly absent from X-ray sources out of synchrotrons. By recording and measuring the distance from the center of the diffraction spots, it is possible to deduce the real lattice geometry and cell parameters. The simplest way revolves around Bragg's law, which states that, given a one-dimensional beam of electrons with wavelength λ impinging on a chain of atoms with interlayer spacing d, positive interference occurs when this relation is satisfied:

$$n\lambda = d \sin(\theta)$$

Given that n represents the diffraction order, the first order of diffraction requires that, given a normal incident angle, which is usually obtained placing the sample right under the electron gun, the

electron wavelength is equal to the surface lattice parameter. Other maxima of diffraction beam intensity can be found at other angles, at subsequent n values as shown below, and are observed as bright spots on a fluorescent screen. In this configuration the zero order of diffraction cannot be observed, as it coincides with the electron gun position[42].

2.5 Electrochemistry

2.5.1 Electrode kinetics theory

The electrode kinetics are studied by means of cyclovoltammetries to obtain two catalytic figures of merit: the exchange current density j_0 and the potential needed to reach the arbitrary current density value of 5 mA/cm^2, which will be called V_5. Other parameters can be found as well: the onset potential, defined as the first potential at which the reaction can occur, represents the bypassing of the thermodynamic barrier and the entrance in the potential region in which the electron transfer is the rate determining step, but there is no single method of calculating it. The Tafel slope, although frequently used, can be an interesting but misleading parameter about the RDS of the reaction. On the other hand, the exchange current density is a strong indicator of the electrode kinetics which can be calculated from the micropolarization region, and

the evaluation of a potential value at an arbitrary current density far from the diffusion limited region allows to compare different samples more reliably.

As described by the Butler-Volmer theory, the exchange current is:

$$j_0 = nFC_0^* K^o exp\left(-\frac{\alpha nF(E_{eq} - E^o)}{RT}\right)$$

It is the current passing through an electrode in both directions when $E = E_{eq}$ or, in other words, when the overpotential and the current density are null. K^o is defined as the standard kinetic constant of electron transfer and, just like the exchange current, is does not depend on applied potential and can be used to compare different electrodic processes at equal temperatures, being solely dependent on the intrinsic activation barrier: $K^o = Zexp\left(-\frac{(\Delta G^{\neq})_0}{RT}\right)$, with Z being a pre-exponential factor which depends on the mass of the reagents and of the products.

As mentioned in the introduction section, the Butler-Volmer equation is the following:

$$j = j_0 \left[exp\left(\frac{(1-\alpha)nF\eta}{RT}\right) + exp\left(-\frac{\alpha nF\eta}{RT}\right)\right]$$

At low overpotential, i.e. close to equilibrium region in which $\eta \ll RT/\alpha nF$, the equation's exponentials can be expanded in series:

$$j = j_0 \left[1 + \frac{(1-\alpha)nF\eta}{RT} - 1 + \frac{\alpha nF\eta}{RT}\right] = j_0 \left[\frac{nF\eta}{RT}\right]$$

The first order derivative of the overpotential with respect to the current density represents the resistance associated with the electron transfer, and its calculation allows to determine the exchange current density:

$$j_0 = \frac{RT}{nF}\left(\frac{\partial\eta}{\partial j}\right)^{-1}$$

2.5.2 Equipment and methods

Electrochemical measurements require the assembly of an electrochemical cell (Figure 2-10a). It is made of three electrodes: the working electrode (WE), onto which the catalyst to study is connected; a counter-electrode (CE), through which the opposite current of the WE passes, so to close the amperometric circuit, which is usually made of an inert conductive material (graphite, in this thesis case); and lastly the reference electrode (RE), an unpolarizable electrode that is used as a reference for the potential applied to the WE and to close the potentiometric circuit. A Hg/HgO electrode (MOE, Mercury Oxide Electrode), suitable for alkaline conditions, was employed. A cell is usually also equipped with an inert

gas inlet, nitrogen for these studies, to degas the solution and eliminate bubbles between the measurements, and with an outlet for the gas which saturates the cell or produced during the experiments. The typical setup is shown in Figure 2-10b.

A KOH 0.1 M solution was used to study the alkaline HER reaction activity, degassed with nitrogen for at least 20 minutes before the measurements. Given the Pourbaix diagram of ruthenium[43], CVs were recorded between 0 and 0.3 V vs RHE at 20 mV/s. After the first ones, 300 cycles in the same range at 500 mV/s were performed to clean the sample of impurities. Linear sweeps to study the HER activity were performed at 10 mV/s between 0.3 and -0.45 V vs RHE. After this, hundreds of aging cycles in the HER range are performed to observe how the activity of the catalyst changes.

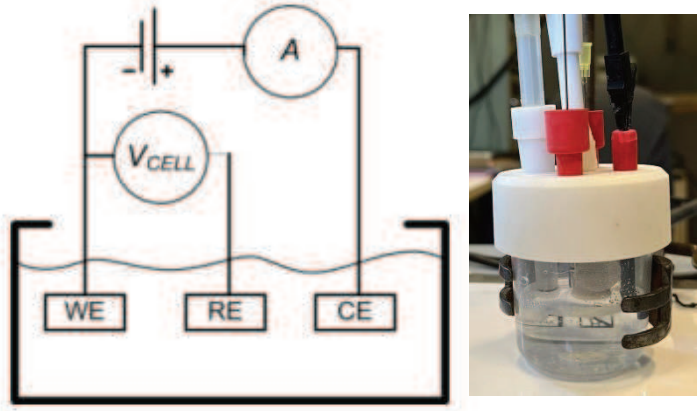

Figure 2-10: (a) scheme of a three electrodes electrochemical cell and (b) typical experimental setup.

3 Chapter 3: Results and discussion

3.1 STM investigation of clean Pt(111) and RuOx/Pt

3.1.1 Clean Pt(111)

The sample was cleaned by cycles of Ar^+ ion sputtering and annealing it in 10^{-6} Torr oxygen pressure to 750°C until no impurities could be detected via XPS and LEED analysis. Typical data are

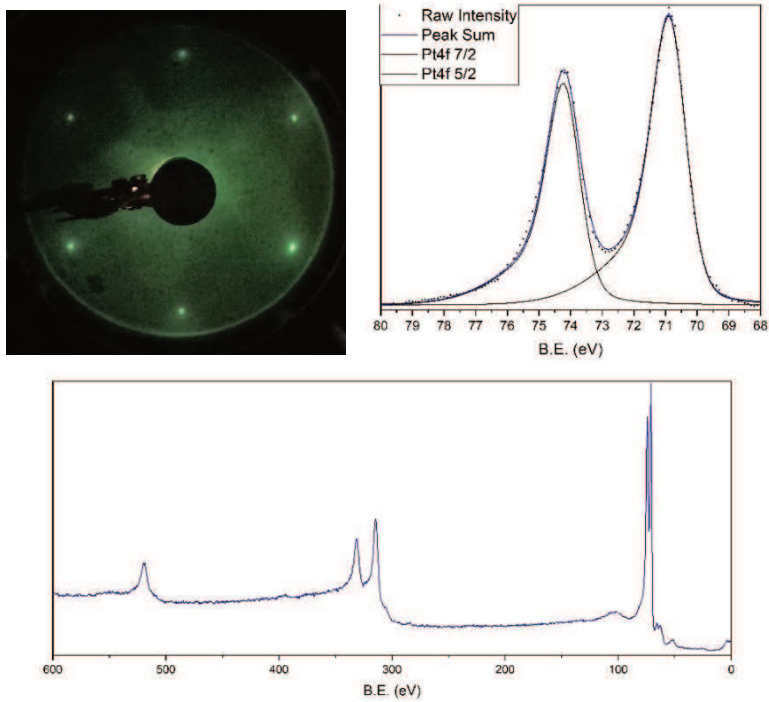

Figure 3-1: on the top left, the Pt(111) LEED pattern (70 eV) obtained after sputtering and annealing cycles. On the bottom, a typical survey of the clean platinum single crystal and, on the top right, the fitted Pt4f peaks.

reported in Figure 3-1, and consist of very sharp LEED pattern and narrow photoemission peaks. The Pt4f peaks were fitted using the XPSPeak software, which does not feature a Doniach-Sunjic line shape[39], but rather asymmetry factors that modify a Voigt curve shape.

When investigated via STM (Figure 3-2), the clean platinum surface appears with sharp terraces of variable sizes depending on the preparation: longer annealing time and higher temperature annealing, typically produce larger terraces.

The height of the step was measured to be around 2 Å, in accordance to the reference values of ∼2.3 Å[44]. The small difference can be attributed to the tip shape, as well as to topological and electronic effects. Atomic resolution images showed a threefold symmetry and long-range order, as the Fast Fourier transform (FFT) and the LEED patterns also do. The surface rhombic unit cell was characterized by a periodicity of 2.83 Å, in good agreement with the literature value of 2.76 Å[45].

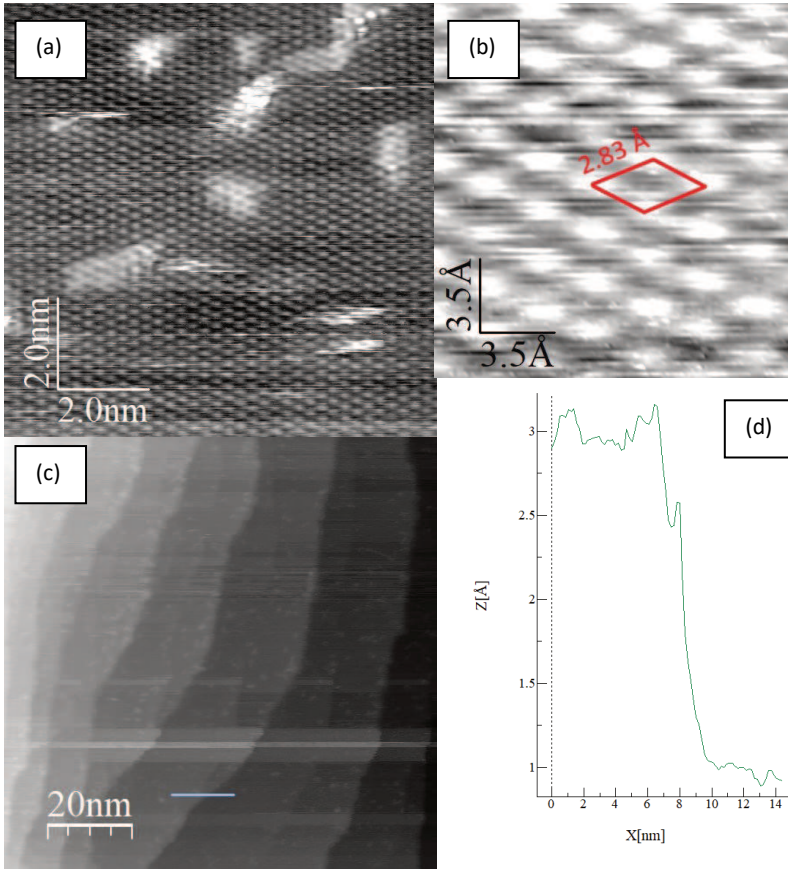

Figure 3-2: STM images of clean Pt(111) at 298 K. (b) is a zoomed version of (a), outlining the unit cell and showing the atomic lattice (I_T = 6.0 nA, V = 50 mV). (c) shows a 100x100 nm^2 image of the crystal (I_T = 2.0 nA, V = 500 mV), and (d) the profile taken along the scanning line.

3.1.2 Deposition

The RuOx/Pt thin films were obtained by thermally activated chemical vapor deposition of a $Ru_3(CO)_{12}$ precursor onto the surface of the platinum crystal in UHV. For all experiments the base pressure was below $5*10^{-9}$ Torr. In similar experiments in the literature[46,47] ruthenium was deposited while keeping the sample at 220°C, then a flux of molecular oxygen was introduced at 300°C to remove the carbon; then the metal ruthenium was reduced with an hydrogen flow at 100 K, and lastly the sample was flashed to 300°C to remove the hydrogen. Flashing and cooling were not possible in the available UHV system, so different routes were tested.

Previous studies on the precursor show that it decomposes partially in the following way[48]:

$$Ru_3(CO)_{12(s)} = (1\text{-}b)Ru_3(CO)_{12(g)} + 3bRu_{(s)} + 12bCO_{(g)}$$

The measured average molecular weight of the metallorganic precursor was 107.58 g/mol, a value much lower than the theoretical value of 639.33 g/mol. In fact, the precursor is unstable, and partially decomposes to CO and solid ruthenium, which is not volatile, near room temperature.

Pt/Ru nanoparticles studies on HOPG supports show[49] that ruthenium has an higher surface energy than platinum and, if heated

above 400°C, the two elements can form an alloy in which platinum is more likely to stay on the very surface. To avoid contamination in the single crystal, the Ru depositions were performed in an oxygen pressure in order to activate the CO oxidation to CO_2 and to anchor the ruthenium to the surface by partially oxidizing it. Two different deposition procedures were performed, named with letters *a* and *b*. The parameters can be found in the table below. The clean platinum sample is first brought to the reported temperature, then it is exposed to molecular oxygen (see Table 1) for five minutes before the precursor valve is opened. After the deposition, the oxygen pressure is maintained for additional five minutes, during which the sample is also cooled down. Given its low vapor pressure, solid $Ru_3(CO)_{12}$ sublimates under UHV condition and forms a molecular beam in the chamber in a molecular flux regime, requiring that the platinum sample to be well aligned with the precursor pocket. Initial tests without oxygen background pressure showed that, upon opening the precursor valve, the pressure in the preparation chamber typically rose to values in the low 10^{-8} Torr. In the following chapter the STM, XPS and LEED data of various samples will be discussed: the number in the sample name will refer to the number of minutes of deposition, while the letter *a* or *b* will refer to the deposition conditions listed below.

Deposition type	Precursor temperature (K)	Sample temperature (K)	Oxygen pressure (Torr)
a	290±10	520±20	$4x10^{-7}$
b	290±10	570±20	$5x10^{-6}$

Table 1: the experimental parameters for the deposition in the two modes are reported.

3.1.3 RuOx/Pt(111) surface and structure

3.1.3.1 Lattice parameters

For every sample, regardless of the oxygen pressure during deposition, deposition time and the size of the adsorbate islands, the

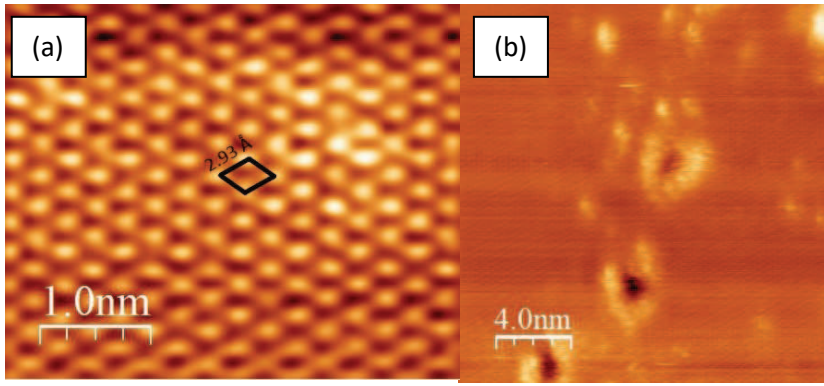

Figure 3-3: (a) room temperature atomic resolution image of the ruthenium adlayers from sample 10b. (I_T = 6.0 nA, V = 60 mV) and (b) a similar, wider image in which pit-like defects can be seen on the ruthenium adislands. The central hole is 1.3 Å deep, consistent with the distance from the underlying platinum substrate which will be discussed in a few paragraphs.

investigated LEED patterns were analogous to the p(1x1) pattern of the clean Pt(111) surface.

In support of this, atomic resolution images of samples 10b and 20b show that RuOx has a hexagonal-like symmetry. The lattice parameter, i.e. the length of the side of the hexagon, has been measured to be equal to 2.93 Å. This value is nearly identical to that of Pt(111), which is reported to be 2.76 Å[45] and, according to our STM measurements, was found to be 2.83 Å. Atomically resolved images have been obtained by finding a wide and flat area of ruthenium covering the substrate and by increasing the tunneling current. Despite the same lattice parameter as platinum, in samples 10b and 20b the ruthenium covered areas were easy to spot thanks to the presence of pit-like defects showing the underlying platinum metal, as Figure 3-3 shows.

3.1.3.2 Coverage

5, 10, 20 and 50 minutes of deposition time were investigated via STM. The coverages were calculated both via measuring the scanned area covered by ruthenium across various images at the same deposition time, and via XPS. Clean platinum has well defined edges, a very smooth surface, only corrugated by occasional carbon contaminations, while no cluster or contamination was ever observed on the RuOx islands. By comparing these images to

the topographies of clean platinum, the adislands can be univocally assigned to RuOx. The random and occasional presence of pits on these clusters, which can be seen on samples 10b and 20b but not on clean platinum, and the characteristic shapes of the adsorbates are two more useful indicators to distinguish the two metals. In general, the adislands nucleate and grow on the lower side of platinum steps. These considerations are the main basis onto which the surface coverage is calculated; however, for the latter reason, the coverage calculation from images with many steps produces different results with respect to images with wider terraces. The small clusters onto the terraces are also excluded from the calculation: if they are stable ruthenium nuclei, the coverage is going to be underestimated. However, because of the

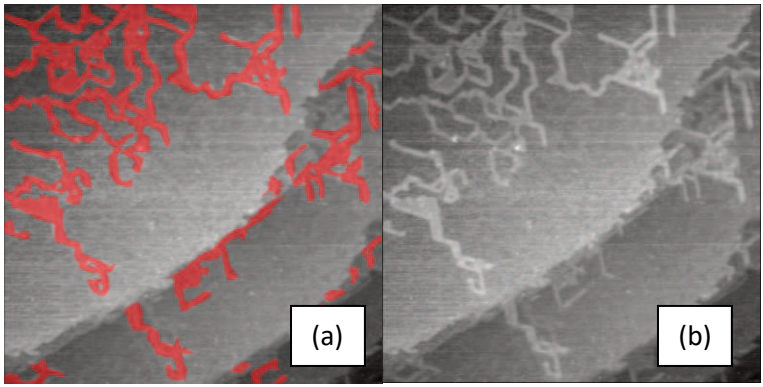

Figure 3-4: 150x150 nm^2 STM image (I_T = 1.0 nA, V = 500 mV) of sample 5b-Nazca, which will be characterized in detail in section 3.1.3.3. In figure (a) the ruthenium adsorbates are coloured in red, and their area is summed and divided by the total area to calculate the coverage. Figure (b) is the original

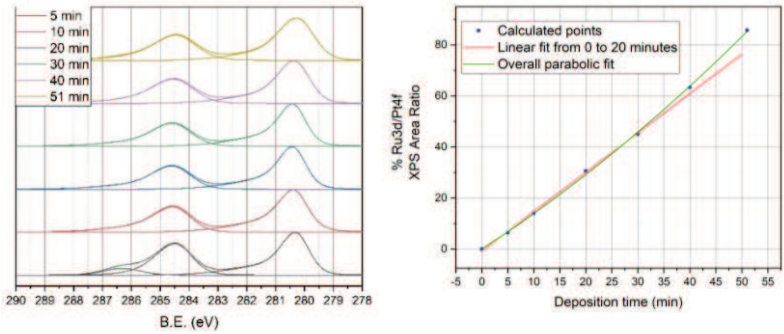

Figure 3-5: on the left, the normalized and vertically shifted fitted peaks for the various deposition times. The Ru3d$_{5/2}$ binding energy fluctuates between in the 280.35±0.07 eV range, and the peaks are less asymmetric as the deposition time increases. A C1s CO peak was necessary to fit the 5 minutes data. On the right, linear and parabolic fit of the Ru3d/Pt4f photoemission peaks area versus deposition time. Out of all the possible fitted straight lines with at least three points, the one which stops at the 20-minute mark has the reduced Chi square closest to one, being 0.19 while all the others don't get past 0.15. This remains true by forcing the intercept at the zero point.

high temperature during the CVD process, it is unlikely that they are ruthenium clusters, since the temperature should favor their diffusion. The coverage so calculated via STM images is reported in Table 2, and an example of the method is shown in Figure 3-4.

Deposition time (min)	5	10	20	50
Average percentage of covered surface	22%	51%	97%	/

Table 2: the calculated fractional coverage of the platinum surface is reported.

The somewhat linear growth of the coverage measured by STM until 20 minutes of deposition time is in good agreement with XPS analysis (see Figure 3-5). Consecutive b-type depositions at 5, 10,

20, 30, 40 and 51 minutes were performed and the Ru3d/Pt4f photoemission peak area ratio was calculated: a reduced Chi square analysis shows that the area ratio follows a line until 20 minutes of deposition, then a parabolic trend better suits the data.

3.1.3.3 Adsorbates morphology and characteristics

The five minute deposition time was investigated multiple times via STM for both deposition types *a* and *b*. At this deposition time, RuOx islands appear as ordered clusters with an apparent corrugation of 2 Å, which as mentioned before grow from the lower side of Pt(111) steps onto which they nucleate. The edges of the adsorbates do not grow in random directions, but rather seem to follow the main directions of the underlying platinum surface. This is

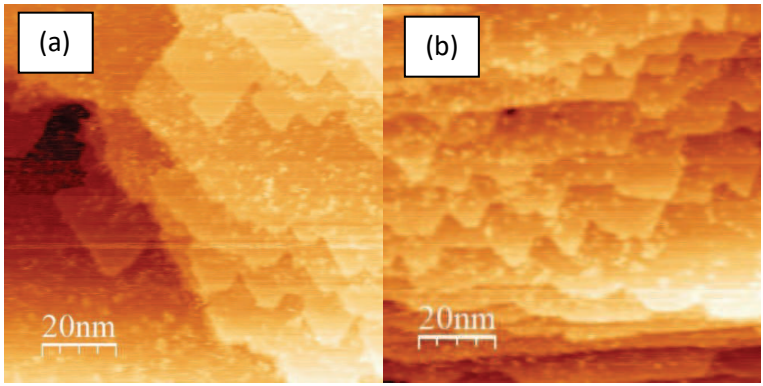

Figure 3-6: STM images of sample 5a-trapezoids, with an average of 22% of surface covered by RuOx, showing wider terraces (a) (I_T = 1.0 nA, V = 500 mV) and more stepped areas (b) (I_T = 3.0 nA, V = 400 mV).

particularly apparent on samples 10b and 5b-Nazca, which will be described in the upcoming section.

At a lower deposition temperature and oxygen pressure, sample 5a (Figure 3-6) exhibits trapezoid-shaped islands growing from the lower side of the platinum steps and small islands, which vary in height between 2 and 3 Å, are observed on the Pt surface.

In the type b deposition, however, three different morphologies were observed with the same synthesis conditions. In the case of sample 5b-triangles, shown in Figure 3-7, the deposited nanostructures took the shape of small, dispersed triangular structures, some of which internally hollow, with a corrugation of about 1.5 Å and with sides long 3 to 4 Å on average. Due to the poor

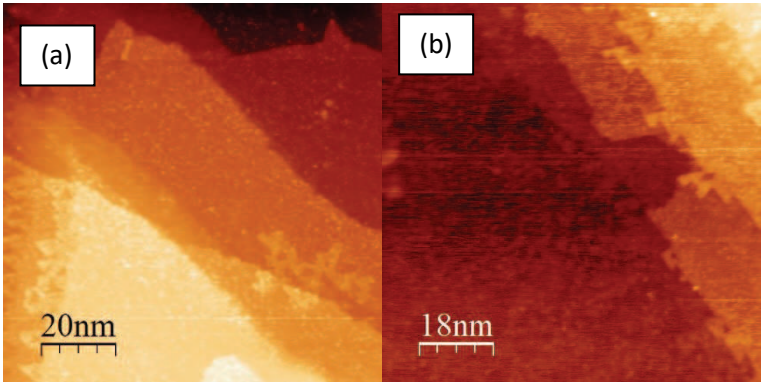

Figure 3-7: STM images of sample 5b-triangles showing triangular shaped adsorbates. In both images (a) (I_T = 2.0 nA, V = 500 mV) and (b) (I_T = 1.0 nA, V = 500 mV), the adsorbates can be seen nucleating and growing from the side of a step and growing along preferred directions in a sort of dendritic fashion. The calculated coverage is around 18%.

quality of the tip, it was impossible to investigate further these structures.

In another STM investigation of sample 5b, peculiar adsorbate structures similar to the Nazca lines were found, characterized by irregular shapes and a few nanometers long (Figure 3-8). These structures are probably of kinetic origin and caused by temperature-limited diffusion. The selected directions of growth suggest that their shape is influenced by the crystalline structure of the substrate, as in the case of a dendritic growth. Small fluctuations in the deposition temperature can induce significant rearrangements of the adsorbates, as similar features have been observed with water adsorbed over Ru(0001) below 150 K[50]. These Nazca-like structures have an apparent corrugation of 2.5 Å and are

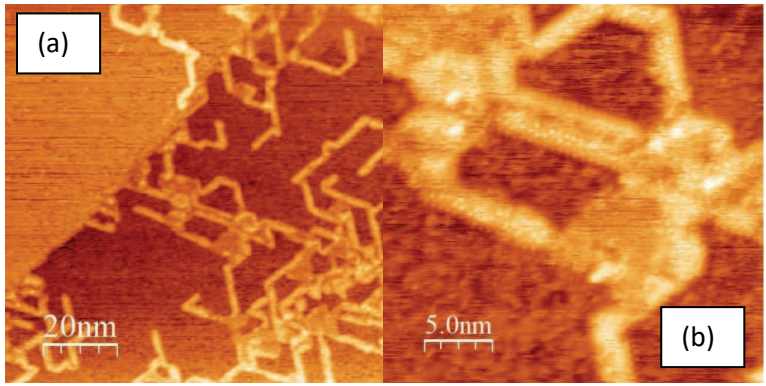

Figure 3-8: STM images of sample 5b-Nazca. Figure (a) (I_T =1.0 nA, V = -500 mV) shows a wider 100x100 nm^2 area, while (b) (I_T = 3.0 nA, V = -500 mV) shows the zoomed in details of the central features of figure (a), in which atomic features can be distinguished.

around 2 nm wide. In the only available image which almost shows atomic resolution (Figure 3-8b), the interatomic distance – measured on the edge of the Nazca line, where it is visible – is measured to be 5 Å. The LEED pattern was identical to that of clean Pt(111): in the hypothesis of 5 Å to be the distance between two atoms in *meta* position on a regular hexagon, the nearest neighbor distance is calculated to be 2.8 Å, which further indicates an epitaxial deposition. This hypothesis is reinforced by the directions along which the lines grow, which strongly resemble the densely packed directions of Pt(111).

A third 5-minute type b deposition (Figure 3-9) was performed, a mixed surface comprising both the trapezoid islands and the Nazca lines. For these reasons, it will be called 5b-MG (Mixed Growth). Due to a higher temperature (1100 K) annealing of platinum, the substrate terraces were wider and the step edges – on which Ruthenium tends to grow – fewer. A lower density of nucleation sites and the deposition temperature uncertainty may be the cause for the mixed growth behavior. Atomically resolved images similar to those of Figure 3-3 and with the same lattice parameter were obtained on the large and smooth ruthenium islands. The Nazca lines showed an apparent corrugation of around 2 Å and 2-3 nm wide, as in the previous case.

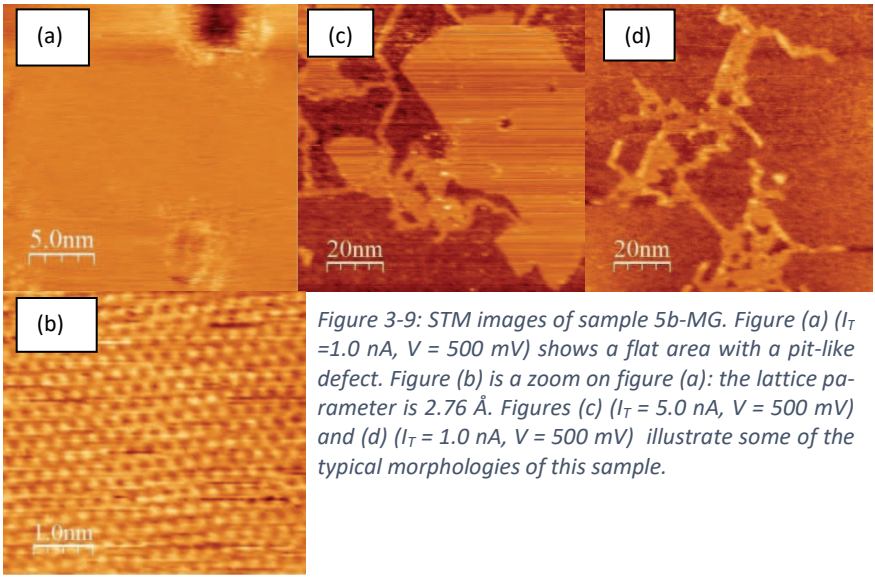

Figure 3-9: STM images of sample 5b-MG. Figure (a) (I_T =1.0 nA, V = 500 mV) shows a flat area with a pit-like defect. Figure (b) is a zoom on figure (a): the lattice parameter is 2.76 Å. Figures (c) (I_T = 5.0 nA, V = 500 mV) and (d) (I_T = 1.0 nA, V = 500 mV) illustrate some of the typical morphologies of this sample.

The XPS analysis (Figure 3-10) of these sample Ru3d photoemission peaks shows the typical features of metallic ruthenium, such as the highly asymmetric $Ru3d_{5/2}$ peak and the absence of RuO_2 satellite peaks, although the binding energy of the main peak, 280.5 eV, falls quite far from both the reported 279.75 eV binding energy of metallic ruthenium and that of RuO_2, 281.37 eV[51]. In another deposition experiment without oxygen background pressure, we measured a metallic $Ru3d_{5/2}$ photoemission binding energy equal to 279.7 eV. A comparison between the normalized high resolution photoemission scans in the Ru3d range of the four 5 minutes depositions with oxygen shows that the 5b-Nazca sample had a positive shift of 0.2 eV of the Ru3d peaks, i.e. 280.5 eV

versus the 280.3 eV of the other three samples, and lower asymmetry factors were needed to fit the data; also, it must be noted that samples 5b-triangles and 5b-MG have higher carbon content

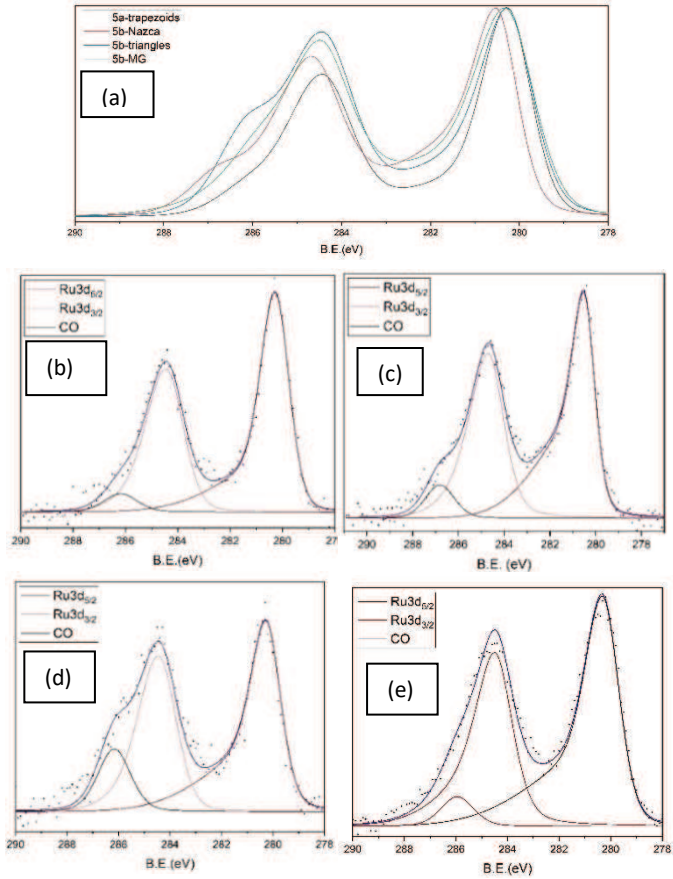

Figure 3-10: XPS analyses of samples 5x. Figure (a) shows the normalized fitted sum of peaks of the three samples. The high-resolution scans of figures (b), (c) (d) and (e) are, in order, those of samples 5a-trapezoids, 5b-Nazca, 5b-triangles and 5b-MG. A higher asymmetry factor for the $Ru3d_{5/2}$ peak was necessary when the binding energy was 280.3 eV, i.e. for all samples but 5b-Nazca.

than the other two. For sample 5b-MG this is also due to previous contamination which couldn't be remove, whereas for sample 5b-triangles this could be a consequence of the progressive decomposition of the precursor, as mentioned before[48]. Given that the four depositions occurred with one month distance between each other (5a-trapezoids > 5b-Nazca > 5b-triangles > 5b-MG), it is plausible that the $Ru_3(CO)_{12(s)}$ decomposed more to $Ru_{(s)}$ and $CO_{(g)}$, lowering the proportion of $Ru_3(CO)_{12(g)}$ with respect to $CO_{(g)}$. This would also explain the lower coverage for sample 5b-triangles, which was measured to be around 18% via STM.

STM images of sample 10b (Figure 3-11) reinforce the idea that the Ru species nucleate on the side of the steps and then grow as

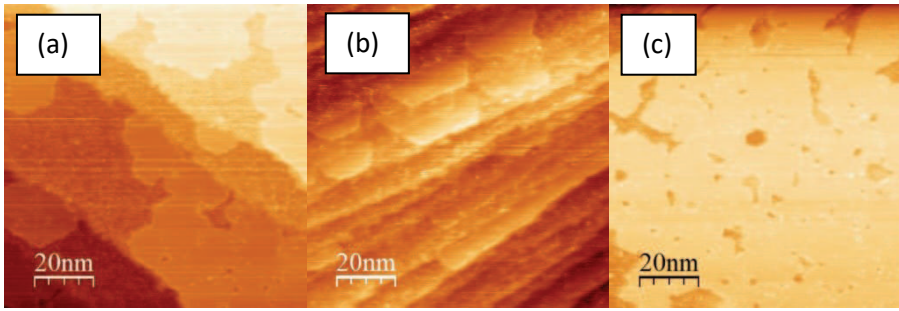

Figure 3-11. Images from sample 10b showing the growth of the adislands on the side of the terrace, with an average of 52% of surface covered by RuOx. In image (a) (I_T = 1.0 nA, V = 200 mV) small pits can be seen in the middle of the adsorbates, while image (b) (I_T = 1.0 nA, V = 200 mV) shows how the adislands grow in a hexagonal symmetry on the small terraces of a step-bunched portions of the sample. Image (c) (I_T = 3.0 nA, V = 200 mV) shows that the adsorbates have already coalesced on a wide terrace, still leaving holes within the island.

islands, mostly in hexagonal symmetry. This can be particularly seen on the regions characterized by step-bunches, but also in areas with wider terraces. In these images, the atomic step between two adjacent Pt terraces is found to be 2.15 Å, compatible with the literature values[44], while the adsorbates lies 1.3 Å (the same as the pits' depth) above the terrace it is deposited on and 0.9 Å below the terrace onto whose step it nucleates. By only considering topological and excluding the electronic effects, this information could lead to the hypothesis that ruthenium may deposit in bridging or hollow sites. On the other hand, the ordered and big islands could plausibly be a consequence of the high deposition temperature, which favours the most thermodynamically stable configuration for adsorbates.

The Ru3d photoemission peaks of sample 10b are very similar to those of sample 5b-Nazca in terms of binding energy of the main peak, which falls at 280.5 eV, while the asymmetry is lower. As mentioned in the Coverage section, as the deposition time increases, the asymmetry factors needed to fit the data tend to decrease. This is also true for sample 20b, whose main photoemission peak falls at 280.5 eV and can be fitted with analogous parameters to sample 10b.

At double deposition time than that of sample 10b, sample 20b (Figure 3-12) shows that the platinum surface has been completely covered. In fact, after nucleating on the side of the steps and growing as islands, different patches coalesce into a continuous film, covering the whole surface of platinum. Albeit blurred, an atomic resolution image was obtained on this sample too, measuring a 2.93 Å atomic distance. Some pits still remain visible, and on top of the first layer small ruthenium clusters with diameters between 1.5 nm and 4.0 nm and 3 Å tall start to appear. The height of the steps results 2.2 Å.

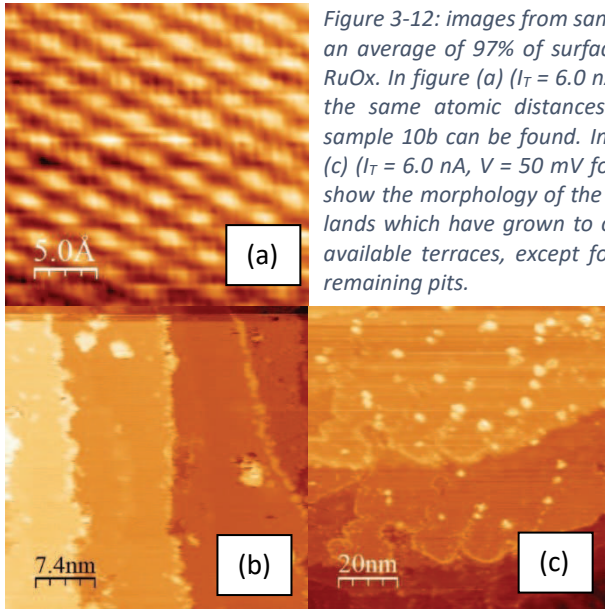

Figure 3-12: images from sample 20b, with an average of 97% of surface covered by RuOx. In figure (a) (I_T = 6.0 nA, V = 50 mV) the same atomic distances as those of sample 10b can be found. Images (b) and (c) (I_T = 6.0 nA, V = 50 mV for all of them) show the morphology of the ruthenium islands which have grown to occupy all the available terraces, except for some small remaining pits.

After the first monolayer is completed, the Ruthenium species adopts a steep and vertical three-dimensional growth, as it can be seen for sample 50b (Figure 3-13): huge pyramid-like structures grow on top of the first flat layer of RuOx in a typical overall Stranski-Kastanov growth. The dark pits of the images above are at least 1.75 nm deep; as shown in the corresponding profile line, the STM tip is too blunt to scan beyond that depth.

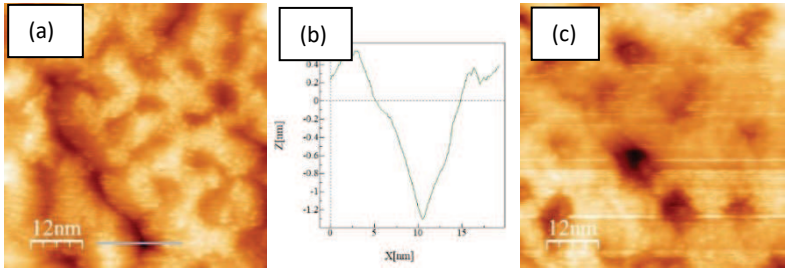

Figure 3-13: (a) and (c) are STM images (I_T = 0.5 nA, V = 200 mV) of sample 50b. The morphology of the sample is highly corrugated. Picture (b) shows the profile outlined in picture (a): given the shape of the profile, it is hard to assess accurately how many layers of RuOx are stacked.

3.1.3.4 CO dosing experiments

CO exposure at room temperature does not alter significantly the STM images. As other works have shown[36], CO can adsorb on top of Ru atoms or, in the case of RuO_2(110), it mildly reduces the oxide by substituting part of the bridging oxygen atoms and adsorbs on top of Ru atoms. Then, the carbon of the adsorbed CO binds a bridging oxygen atom, forming an unstable intermediate which is

stabilized as the molecule forms a second double C=O bond, desorbing from the oxide as CO_2 and leaving an oxygen vacancy. This kind of mechanism requires the oxygen to be exposed on the surface, and therefore the bulk oxygen atoms are unaffected by it.

The samples 50b and 10b were exposed to CO. 10 Langmuir (L) of CO gas were fluxed on sample 50b in the prep chamber (Figure 3-14). An XPS measurement showed that the BE of $Ru3d_{5/2}$ shifted upward by an amount smaller than the experimental error. Afterwards, the sample was heated to around 600 K: a subsequent XPS measurements revealed that, as expected, RuOx was partially reduced, with its BE shifting downward by 0.2 eV, to 280.1 eV.

In the case of sample 10b (Figure 3-15), CO was dosed three consecutive times, 50 L, 50 L and 550 L. The much greater amount of CO is justified by the geometry of the STM chamber, in which the sample faces in the opposite direction relatively to the gas source and towards a pit in which the tungsten tip dwells. In all these three cases, no new oxygen vacancies nor new holes were detected, and CO did not form any clearly visible reconstruction over the catalyst surface, but instead some pits and holes seem to close. An XPS analysis followed the STM measurements, showing that the Ru3d BE had shifted from 280.5 to 280.3 eV and that the carbon 1s signals had increased in intensity. After annealing at 600

K, the sample was examined again via XPS, showing that the Ru3d BE had significantly shifted from 280.3 eV to 279.8 eV and that the O1s signal had nearly disappeared. Having also measured that the lattice step of these submonolayer adsorbates is compatible with the one of Pt(111), given that every LEED experiment always showed a p(1x1) pattern of Pt(111), it is reasonable to infer that ruthenium grows epitaxially over Pt(111), forming a strained Ru(0001) layer with the same lattice parameters as platinum and with a slight expansion from its bulk value. On the other hand, oxygen is likely chemisorbed on the Ru layer and without forming a bulk oxide, at least for most of the considered samples. Given the amount of ruthenium on sample 50b and how its BE shifts only by 0.3 eV after the exposure to CO and the annealing, it can be

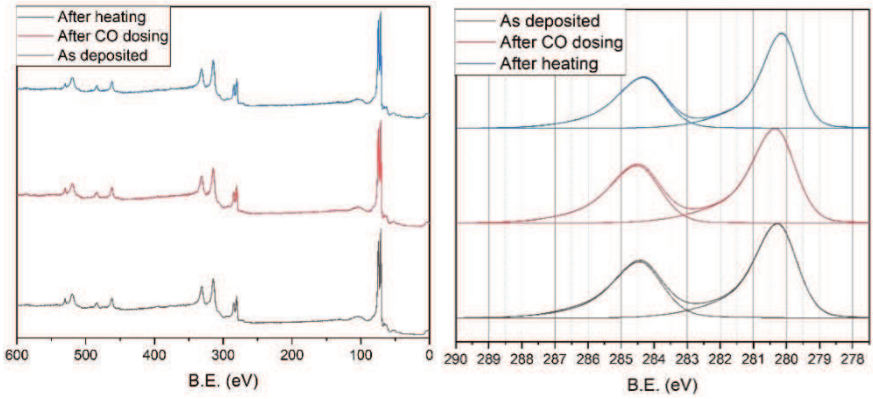

Figure 3-14: normalized XPS spectra of sample 50b before and after exposure to 10 L of CO and after a UHV annealing at 600 K. The surveys on the left show that the amount of oxygen decreases slightly after the annealing, and the high-resolution scans on the right show that the Ru3d peaks negatively shift by 0.2 eV after the annealing.

assumed that beyond a 2ML coverage some of the oxygen is not exposed, but rather in a bulk position. This deduced elemental composition and chemical state of the adsorbate is in line with some studies by Over et al.[33], according to which the formation of a RuO_2(110) thin film over a Ru(0001) surface requires temperatures above 600 K and an uptake of at least 10 ML of O_2 over clean Ru. This can be achieved by an excessive exposure to oxygen in the order of 10^5 L, with doses of 10^{-2} bar for several minutes. On the other hand, oxidizing experiments on sample 50b with up to 3000 L of dosed oxygen at around 600 K did not bear any significant shift in the Ru3d photoemission peak BE, nor did they change the LEED pattern from the constantly observed 1x1 of Pt(111) to anything different.

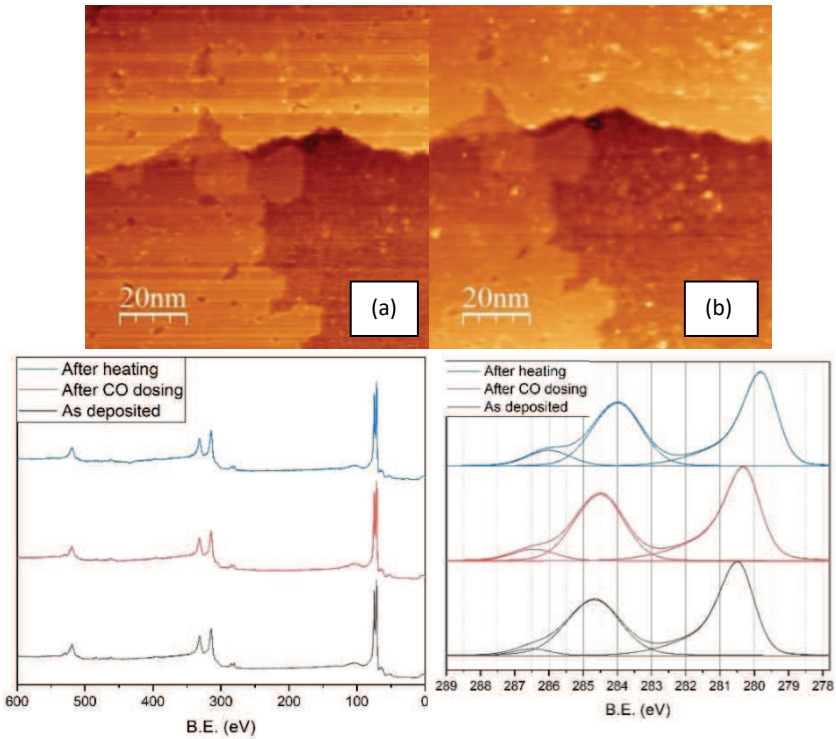

Figure 3-15: On the top, image of sample 10b before (a) and after (b) exposure to 650 L of CO. While the most prominent features did not change, some pits and holes are no longer visible. On the bottom, normalized XPS spectra of sample 10b before and after exposure to 650 L of CO and after a UHV annealing at 600 K. The surveys on the left show that the amount of oxygen decreases after the annealing, and the high-resolution scans on the right show that the Ru3d peaks negatively shift by 0.5 eV after the annealing.

3.1.3.5 Bias switching experiments

During the acquisition of STM images, some bias switching experiments were performed to investigate the behavior of the sample under different bias potentials.

Those in Figure 3-16 are topographic 150x150 nm^2 STM images of sample 5b-Nazca, all of them collected in 2'46'' at a tunneling current equal to 4.0 nA: image (a), with a positive bias of 500 mV, shows the typical features of sample 5b-Nazca, with long lines of RuOx around 4 nm wide and corrugated of 1.5 Å. As soon as the bias is switched from +500 mV to -500 mV, however, the lines start to fade (b) and eventually the images stabilize to what (c) shows, hiding the steps and the terraces and manifesting a valley among two hilly areas. The current images are analogous. When the bias is switched again to +500 mV (d), the Nazca lines gradually reappear and, after a few minutes, the image stabilizes back to how it originally was (e), proving the sample did not change its morphology.

When this same experiment was tested on samples 20b and 50b, which have respectively around 1 and 2.5 ML of coverage, the adsorbates did not disappear nor changed shape, but the images simply remained like those showed in a previous section. This could either be caused by the peculiar morphology of sample 5b-Nazca or by the fact that, with a lower coverage, it is easier to draw a significant portion of the electrons in a specific band to the point where it is empty, changing how the orbitals are perceived by the tungsten tip.

Although ruthenium is a metal, this kind of behavior could be caused by the probably chemisorbed oxygen over it, which is altering the electronic structure of the system.

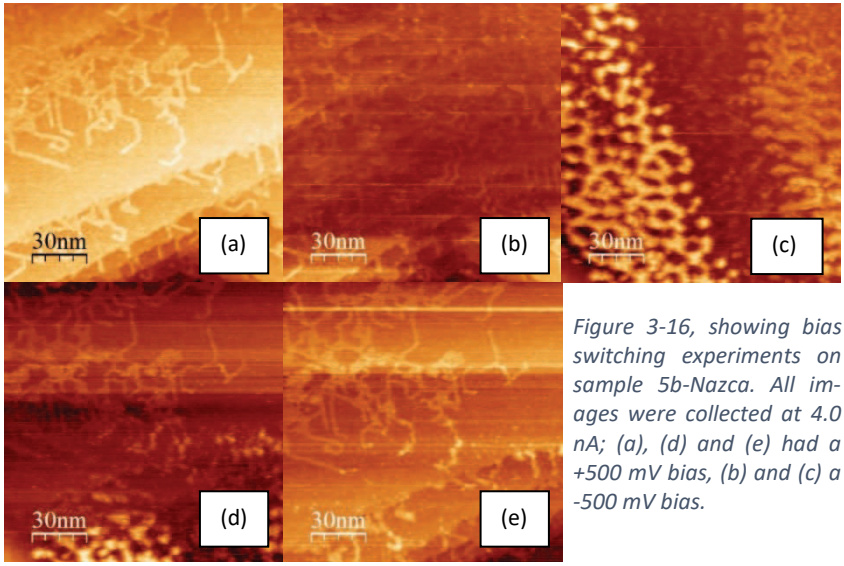

Figure 3-16, showing bias switching experiments on sample 5b-Nazca. All images were collected at 4.0 nA; (a), (d) and (e) had a +500 mV bias, (b) and (c) a -500 mV bias.

3.2 Electrochemical characterization

3.2.1 Premises

As mentioned in section 2.5.2, the samples were tested for alkaline HER activity with a static working electrode in a nitrogen saturated plastic cell, having MOE as a reference electrode and a graphite counter-electrode.

Probably because of some yet to clarify problems in the experimental setup, possibly related to resistance, the initial CVs appeared very steep in the non-faradaic regions, making the study of the adsorption of H and OH quite difficult. An example is reported

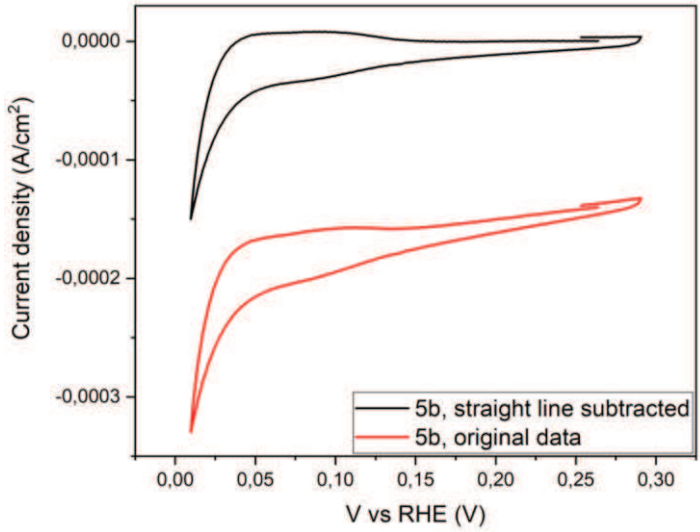

Figure 3-17: example of the steepness of CVs far from the faradaic area.

in Figure 3-17: the current is significantly different from zero in all regions, and the capacitive zone is steeped instead of flat. This problem was not solved by iR compensation, which was applied, since it is mostly relevant at high current values and only shifts the measured potential. All samples also showed a significant shift in their open circuit potential as they were cycled, on average from 0.9 V vs RHE to 0 V vs RHE.

Good quality cyclovoltammetries of Pt(111) (Figure 3-18), very similar to those available in literature[16], were obtained despite these problems, allowing to calculate the electrochemical surface

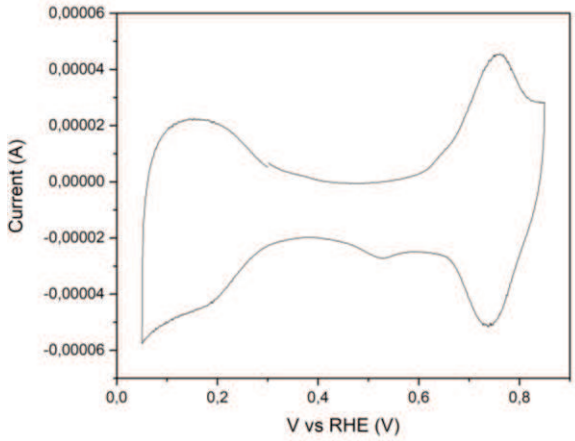

Figure 3-18. Static electrode Pt(111) cyclovoltammetry in KOH 0.1 M, collected at 100 mV/S. On the left the two adsorption peaks of H can be clearly seen; the steepness of the adsorption one is given by internal resistances and a steeped baseline was used to calculate its charge. On the right, the peaks related to the reversible adsorption of OH. The smaller peak at 0.55 V is associated to the reduction of the platinum oxide which starts right after the OH adsorption.

area (ECSA) from the adsorption and desorption of H and OH. Given the little corrugation of a single crystal, the ECSA was predictably of the same order of magnitude of the geometric surface area, respectively 0.214 and 0.502 cm^2. Because of the smaller error which can be made in the measurement of the geometrical surface area, it was used to normalize the current values to current density.

A first batch of measurements, that will be represented with dashed lines, were carried on cycling the samples at potentials at which ruthenium is known to form soluble species. At pH 13, between -0.15 V vs RHE and 0 V vs RHE, Ru is known to form the hydrated hydroxide $Ru(OH)_3 \cdot H_2O$, while below -0.15 V vs RHE it maintains its metallic form[43]. Above 0 V vs RHE and below 0.3 V vs RHE it oxidizes to $RuO_2 \cdot 2H_2O$, and beyond that potential its soluble phases are formed, starting with RuO_4^{2-}. Although these phase changes should be reversible, the partial solubilization of an adsorbate is surely going to change the morphology that had been observed via STM scans, even if Ruthenium can be deposited again on the platinum substrate when switching to negative potentials.

A second batch of samples, represented with solid lines, was only exposed to potentials at which Ruthenium does not form soluble phases.

Given the high carbon content that deposits on the sample outside of the UHV system and given the C1s overlap with the $Ru3d_{3/2}$ photoemission peaks, it is difficult to quantify how much ruthenium may have left the surface. This is also caused by the fact that the first layers investigated by the XPS are no longer made of ruthenium and platinum, but of carbon, water, and ruthenium, due to environmental contamination. As a consequence, the signal from the underlying platinum is lowered due to the longer path the photoelectrons need to travel to be analyzed, and quantitative estimations of how much, if any, ruthenium has been lost while applying potentials above the solubilizing ones are not possible. By comparing the as deposited and the post-EC XPS surveys, after normalizing the data per scan numbers, dwell time and by the $Pt4f_{7/2}$ peak, however, the $Ru3d_{5/2}$ signals are compatible before and after the EC both in terms of BE and

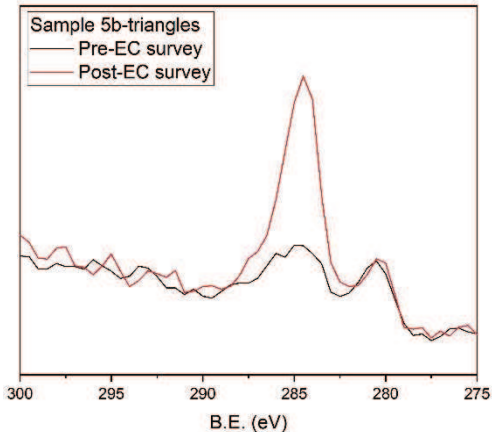

Figure 3-19: comparison between the as deposited and the after-electrochemistry surveys of sample 5b-triangles, which was not exposed to solubilizing potentials.

peak shape, as exemplified by the 5b-triangles sample, as shown in Figure 3-19.

3.2.2 Catalytic Activity

Figure 3-20 reports the linear sweep voltammetries for the tested model catalysts. At first glance, it is evident that very small amounts of ruthenium drastically improve the alkaline HER catalysis, such as in the cases of samples 5a and 5b-triangles, whereas too high amounts inhibit the activity below that of platinum, as sample 50b demonstrates. However, as these RuOx/Pt catalysts are aged (dotted lines), their activity drops below that of clean Pt(111). This is possibly due to the reorganization of the adsorbates on the substrate, whose morphology is subjected to change as different phases form at different potentials. This could lead to reconstructions which, however, were not detected by LEED as the samples were put back into the UHV system. EC-STM measurements are useful to understand how the surface morphology changes during electrochemistry and could be attempted in the future. Two different samples 10b were tested: the one belonging to the second batch (10b-bis) drastically reduced its catalytic activity during the activation scans, with its onset negatively shifting to around -0.22 V. In fact, while the first CV of sample 10b-bis

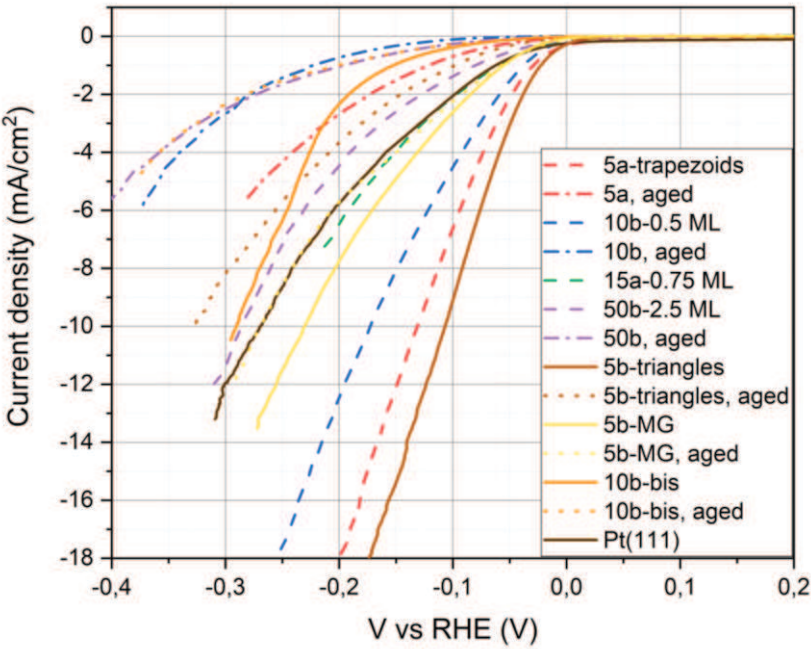

Figure 3-20: hydrogen evolution LSVs for the various tested catalysts. All of them were collected at room temperature, with a static electrode, in a 0.1 M KOH solution. Dashed lines belong to the first batch of samples, which have experienced potentials capable of solubilizing ruthenium, while dotted lines belong to aged samples.

showed some adsorption feature at 0.075 V, after the first few activation cycles and right before the LVS for HER the cyclovoltammetry flattened.

As mentioned by Schmidt et al.[16], depending on the way the Tafel tangents are drawn almost any slope value between 40 and 200 mV/dec can be obtained. This is due to the difficulty of clearly and

univocally defining a Tafel region. Because of this, the micropolarization region, within a small potential interval of the thermodynamic potential, can be taken advantage of to determine the exchange current density j_0, as mentioned in section 2.5.1. Schmidt et al.[16], working with platinum single crystals and with a rotating disk electrode (RDE) spinning at 2500 rpm, fitted their data in the 0±20 mV region, finding an exchange current density j_0 equal to 0.01 mA/cm^2 for Pt(111) and equal to 0.125 mA/cm^2 for Pt(110).

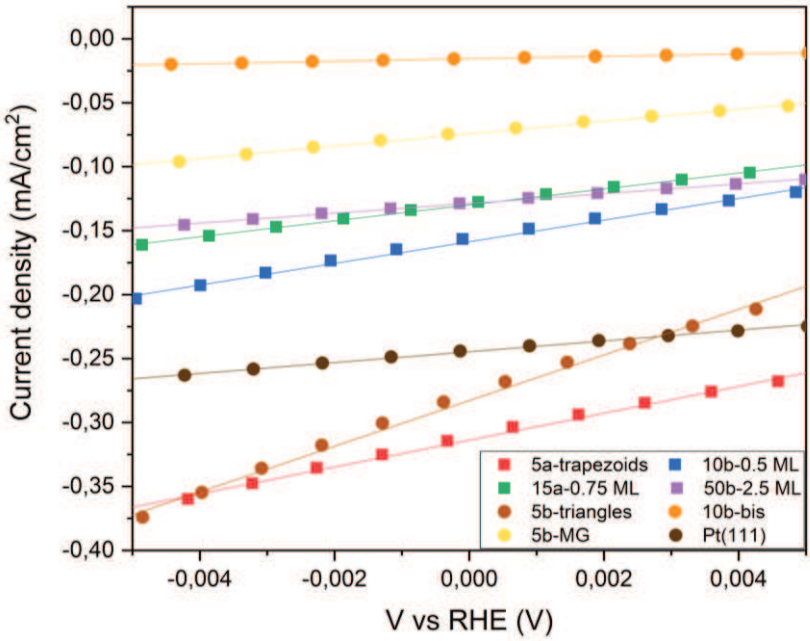

Figure 3-21: the micropolarization region ±5 mV of the reversible potential on the various tested catalysts at room temperature in KOH 0.1 M, 10 mV/s.

However, our data were not linear in that range, which had to be shrunk to 0±5 mV vs RHE (i.e. where is the thermodynamic potential of the reaction) to have a linearity sufficient for and adjusted R_0 above 0.995. Moreover, the experimental data did not intercept the 0 mA/cm^2 current value at 0 V vs RHE, probably for capacitive effects, as shown in Figure 3-21. However, since the slope is independent of the vertical shift of the curve, that should not be a problem. Table 3 reports the calculated j_0, the potential needed to reach a 5 mA/cm^2 current density and the Tafel slope for the investigated samples. The exchange current density was also calculated from the intercept of the Tafel fitting line, but it was not comparable to the micropolarization values and quite far from the literature values.

	j_0 (mA/cm^2)	V_5 (mV)	Tafel slope (mV/dec)	j_0 from Tafel (mA/cm^2)
Pt(111)	0.05	-180	42	0.35
Pt(111) (ref 16)	0.01	-	50	-
5a-trapezoids	0.14	-80	32	0.68
10b-0.5 ML	0.11	-110	36	0.65

15a-0.75 ML	0.08	-200	71	0.69
50b-2.5 ML	0.05	-210	32	0.55
5b-triangles	0.22	-70	44	0.74
5b-MG	0.06	-152	45	0.53
10b-bis	0.01	-240	42	0.10

Table 3: exchange current density j_0 (calculated by linearly fitting the data in the micropolarization region), potential needed to reach 5 mA/cm^2 V_5 and Tafel slope, determined in the electron transfer limited region of the LSVs.

Firstly, it is evident that the HER reaction is strongly sensitive to the morphology and to the sample history. The Pt(111) sample has an exchange current density five times higher that reported in the literature[16], however the mismatch can be attributed to the surface area calculation. The Tafel slope values are plausibly not to be trusted: if the values were accurate, the rate determining step of alkaline HER for clean Pt(111) would not be the Volmer reaction, i.e. the dissociative adsorption of water, but rather something in between the Tafel and the Heirovsky steps, which is in contrast with experimental[9,16] and computational studies[12]. At the same time, the slightly better Tafel slopes for 5a and 5b RuOx/Pt catalysts if compared to the literature can be explained by the presence of an oxyphilic metal which, being capable of forming oxyhydroxides, can lower the energy barrier for the Volmer step[11].

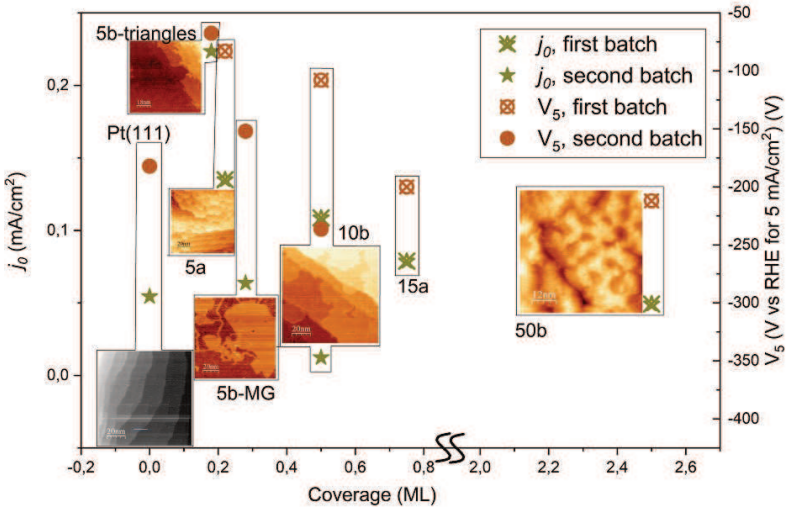

Figure 3-22: scatter plot correlating coverage, morphology, exchange current density and V_5 of the tested samples.

Figure 3-22 shows how the coverage and the morphology affects the catalysis. On the left Y axis one can see the scale of the exchange current density, represented by dark yellow stars in the graph that are crossed if they belong to the first batch of measurements. Similarly, the right Y axis and the copper-colored circles indicate the V_5 parameter, and in this case the hollow crossed circles refer to the first batch. To keep the graph in a smaller horizontal size, as the X axis suggests the area between 0.8 and 2.0 ML was cut. Still bearing in mind that the first batch of samples is potentially not reliable, a volcano plot emerges correlating low coverage and small islands or ruthenium to better performances, in agreement to a very recent article by Zhu et al. who found a similar

correlation between coverage and exchange current density[25]. In particular, the best activity belongs to the sample with the lowest coverage (5b-triangles) for all of the displayed indicators, but not in terms of Tafel slope (see Table 3). As shown in section 3.1.3.3, sample 5b-triangles had very dispersed triangular-shaped Ru islands, some of which having an internal hollow core, with a large interfacial area between platinum and ruthenium, as in the case of the experiments by Xue et al.[21]. For other samples, these features are absent in favor of wider and wider islands, and the catalytic activity decreases: as the coverage grows, the fraction of ruthenium atoms fully coordinated by other ruthenium atoms on the horizontal plane grows as well.

This factor was further investigated by fractal dimensions evaluations carried out on samples 5a-trapezoids, 5b-triangles and 5b-MG. The fractal dimension *D* of a surface is a way of describing its geometric complexity and roughness. The topological dimension of a surface is 2, however as the complexity of a surface grows so does its fractal dimension, which is a non-integer value between 2 and 3[52]. It can be measured via STM, as demonstrated by Gómez-Rodríguez et al.[53], by plotting the measured perimeter of the adsorbates versus their areas. The plot can be fitted with an exponential function:

$$P = \mu A^{\alpha}$$

Where *P* is the perimeter measured in Ångstrom, μ is a pre-exponential fitting factor, *A* represents the areas in nm^2. The fractal dimension *D* is given by $2\alpha+1$. This method overestimates the fractal dimension of a surface, but for more complex surfaces the experimental *D* values get closer and closer to their theoretical counterparts. The fractal dimension of samples 5a-trapezoids, 5b-triangles and 5b-MG were calculated to be 2.2, 2.4 and 2.4 respectively. From the literature, it is known that the ideal catalyst should be fractal[54]: since the fractality is directly correlated to the interfacial area between ruthenium and platinum, better performances of the most fractal would be and indicator of the presence of a bifunctional mechanism. However, sample 5b-triangles and 5b-MG have the same fractal dimension and different activity. The two samples are particularly different for the dimension of the adsorbates and the coverage: the smaller, fewer and more disperse islands of sample 5b-triangles seem to be more effective than the wider and slightly more abundant ones of sample 5b-MG. In absence of further computational studies doing the necessary calculations, it is also possible to hypothesize that the wider ruthenium islands have a stronger electronic modulation effect on platinum than the small ones; this would be a further indication for the

better catalytic improvement in lower coverage samples coming from a bifunctional effect in which ruthenium aids platinum by splitting water, which is particularly good at[10,22], and the nearby platinum atoms catalyze the evolution of hydrogen. This mechanism would be hindered at higher coverages by the lower interfacial area, and the smaller exposed platinum surface area probably has a part too in the worse performances.

However, albeit being very active, such structures are evidently unstable, as discussed before and shown in Figure 3-20; an interesting future experiment could be the deposition of a stable sp^2 carbon layer made of graphene over such catalysts, to investigate whether it can boost their durability without hindering their activities, as some have already attempted[55,56].

4 Conclusions and future outlooks

Mildly oxidized ruthenium, deposited via thermally activated CVD of the $Ru_3(CO)_{12}$ precursor onto a Pt(111) single crystal, was observed forming multiple different epitaxial nanostructures depending on the coverage, on the oxygen pressure and on the platinum temperature during the deposition. The growth mode was found to be a Stranski-Kastanov, with clusters of various shapes nucleating and growing from the lower side of platinum step edges into flat and wide terraces; after the first monolayer is formed, the growth follows a 3D islanding mode.

Static electrode electrochemical measurements in a KOH 0.1 M electrolyte, despite some experimental issues, exposed a greatly increased electrocatalytic activity towards the HER when platinum was covered by small amounts of RuOx. Out of the two best performing samples, the one with the higher fractal dimension was also the better for the two considered electrocatalytic figures of merit, suggesting a bifunctional mechanism between Ru and Pt, respectively better at dissociating water and evolving hydrogen.

One of the investigated samples, named 5b-Nazca, had very interesting line-shaped nanostructures with a great amount of interfacial area between the platinum and the ruthenium. The preliminary tests on a similar sample (5b-MG) did not show a strikingly

better activity than the other samples. This suggests that the coverage and the adislands dimensions play an important role alongside their morphology in boosting the activity of platinum.

An interesting outlook for future studies would be trying to understand which processes make the CVs and the activity of these single crystal-based catalyst change so dramatically, for example by observing the surface morphology via EC-STM. Covering such a system with a graphene layer would also be interesting because it is known to increase the durability of catalysts without significantly impacting their activity, given a number or layers between one and three[55,56]. Given the chemisorbed oxygen on Ru and the high reactivity toward water dissociation this combination is known to have[22], it would also be interesting to study the catalyst activity in-situ to investigate the Ru3d chemical shift after the contact with alkaline water and after electrochemical CVs, without exposing the sample to the atmosphere: this would provide an insight to the stability of this chemical state which, if found to be low, would be another reason to try covering it with graphene.

Some considerations must be made regarding the method. For reasons yet to unveil, the cyclovoltammetries often present themselves as steeply sloped at the beginning of EC measurements. Given that, in our research group, this problem has only been

spotted with the single crystal sample holder and good CVs have proven to be unusually tricky to obtain, before proceeding to further research it is necessary to solve this problem which could lie in the EC cell configuration itself, in the single crystal sample holder or maybe in the in-vacuum preparation of the sample.

Another critical element of this work is the reproducibility. Only a few samples could be tested for electrochemistry due to time constraints and the long preparation that a single crystal requires in UHV to achieve a high-quality surface: because of this, it was not possible to test multiple times the same type of sample, nor to observe them at the STM, the tip of which is often the factor determining whether a good resolution can be achieved.

5 Overall references

1. Yoro, K. O. & Daramola, M. O. Chapter 1 - CO2 emission sources, greenhouse gases, and the global warming effect. in *Advances in Carbon Capture* (eds. Rahimpour, M. R., Farsi, M. & Makarem, M. A.) 3–28 (Woodhead Publishing, 2020). doi:10.1016/B978-0-12-819657-1.00001-3.
2. Hansen, J., Ruedy, R., Sato, M. & Lo, K. Global Surface Temperature Change. *Rev. Geophys.* **48**, (2010).
3. Global Energy Review: CO2 Emissions in 2021. 14 (2021).
4. Gandía, L. M., Oroz, R., Ursúa, A., Sanchis, P. & Dieguez, P. Renewable Hydrogen Production: Performance of an Alkaline Water Electrolyzer Working under Emulated Wind Conditions. *Energy Fuels* **21**, (2007).
5. Wang, M., Wang, Z., Gong, X. & Guo, Z. The intensification technologies to water electrolysis for hydrogen production – A review. *Renew. Sustain. Energy Rev.* **29**, 573–588 (2014).

6. Buttler, A. & Spliethoff, H. Current status of water electrolysis for energy storage, grid balancing and sector coupling via power-to-gas and power-to-liquids: A review. *Renew. Sustain. Energy Rev.* **82**, 2440–2454 (2018).
7. Rashid, M., Mesfer, M. K. A., Naseem, H. & Danish, M. Hydrogen Production by Water Electrolysis: A Review of Alkaline Water Electrolysis, PEM Water Electrolysis and High Temperature Water Electrolysis. **4**, 14.
8. Zheng, J., Sheng, W., Zhuang, Z., Xu, B. & Yan, Y. Universal dependence of hydrogen oxidation and evolution reaction activity of platinum-group metals on pH and hydrogen binding energy. *Sci. Adv.* **2**, e1501602 (2016).
9. Zheng, Y., Jiao, Y., Vasileff, A. & Qiao, S. The Hydrogen Evolution Reaction in Alkaline Solution: From Theory, Single Crystal Models, to Practical Electrocatalysts. *Angew. Chem. Int. Ed.* **57**, 7568–7579 (2018).

10. Schwämmlein, J. N. *et al.* Origin of Superior HOR/HER Activity of Bimetallic Pt-Ru Catalysts in Alkaline Media Identified via Ru@Pt Core-Shell Nanoparticles. *J. Electrochem. Soc.* **165**, H229–H239 (2018).
11. Li, J. *et al.* Experimental Proof of the Bifunctional Mechanism for the Hydrogen Oxidation in Alkaline Media. *Angew. Chem. Int. Ed.* **56**, 15594–15598 (2017).
12. Durst, J. *et al.* New insights into the electrochemical hydrogen oxidation and evolution reaction mechanism. *Energy Env. Sci* **7**, 2255–2260 (2014).
13. De Silva, Y. & Middleton, P. Design of an Alkaline Electrolysis Stack. (2017). doi:10.13140/RG.2.2.14351.12964.
14. Brauns, J. & Turek, T. Alkaline Water Electrolysis Powered by Renewable Energy: A Review. *Processes* **8**, 248 (2020).
15. Mahmood, N. *et al.* Electrocatalysts for Hydrogen Evolution in Alkaline Electrolytes: Mechanisms, Challenges, and Prospective Solutions. *Adv. Sci.* **5**, 1700464 (2018).

16. Schmidt, T. J., Jr, P. N. R. & Markovic, N. M. Temperature dependent surface electrochemistry on Pt single crystals in alkaline electrolytes Part 2. The hydrogen evolution/oxidation reaction. *J. Electroanal. Chem.* 9 (2002).
17. Łosiewicz, B., Jurczakowski, R. & Lasia, A. Kinetics of hydrogen underpotential deposition at polycrystalline platinum in acidic solutions. *Electrochimica Acta* **80**, 292–301 (2012).
18. Lamoureux, P. S., Singh, A. R. & Chan, K. pH Effects on Hydrogen Evolution and Oxidation over Pt(111): Insights from First-Principles. *ACS Catal.* **9**, 6194–6201 (2019).
19. Marković, N. M. *et al.* Effect of Temperature on Surface Processes at the Pt(111)−Liquid Interface: Hydrogen Adsorption, Oxide Formation, and CO Oxidation. *J. Phys. Chem. B* **103**, 8568–8577 (1999).
20. Subbaraman, R. *et al.* Enhancing Hydrogen Evolution Activity in Water Splitting by Tailoring Li^+-$Ni(OH)_2$-Pt Interfaces. *Science* **334**, 1256–1260 (2011).

21. Xue, S. *et al.* Enhancing the Hydrogen Evolution Reaction Activity of Platinum Electrodes in Alkaline Media Using Nickel–Iron Clusters. *Angew. Chem. Int. Ed.* **59**, 10934–10938 (2020).
22. Shavorskiy, A., Gladys, M. J. & Held, G. Chemical composition and reactivity of water on hexagonal Pt-group metal surfaces. *Phys. Chem. Chem. Phys.* **10**, 6150–6159 (2008).
23. Strmcnik, D. *et al.* Improving the hydrogen oxidation reaction rate by promotion of hydroxyl adsorption. *Nat. Chem.* **5**, 300–306 (2013).
24. Subbaraman, R. *et al.* Trends in activity for the water electrolyser reactions on 3d M(Ni,Co,Fe,Mn) hydr(oxy)oxide catalysts. *Nat. Mater.* **11**, 550–557 (2012).
25. Zhu, S. *et al.* The role of ruthenium in improving the kinetics of hydrogen oxidation and evolution reactions of platinum. *Nat. Catal.* **4**, 711–718 (2021).
26. Hodgson, A. & Haq, S. Water adsorption and the wetting of metal surfaces. *Surf. Sci. Rep.* **64**, 381–451 (2009).

27. Koper, M. T. M. Blank voltammetry of hexagonal surfaces of Pt-group metal electrodes: Comparison to density functional theory calculations and ultra-high vacuum experiments on water dissociation. *Electrochimica Acta* **56**, 10645–10651 (2011).
28. Lunardon, M., Kosmala, T., Durante, C., Agnoli, S. & Granozzi, G. Atom-by-atom identification of catalytic active sites in operando conditions by quantitative noise detection. *Joule* **6**, 617–635 (2022).
29. Kosmala, T. *et al.* Operando visualization of the hydrogen evolution reaction with atomic-scale precision at different metal–graphene interfaces. *Nat. Catal.* **4**, 850–859 (2021).
30. Strbac, S., Johnston, C. M., Lu, G. Q., Crown, A. & Wieckowski, A. In situ STM study of nanosized Ru and Os islands spontaneously deposited on Pt(111) and Au(111) electrodes. *Surf. Sci.* **573**, 80–99 (2004).

31. Herrero, E., Feliu, J. M. & Wieckowski, A. Scanning Tunneling Microscopy Images of Ruthenium Submonolayers Spontaneously Deposited on a Pt(111) Electrode. *Langmuir* **15**, 4944–4948 (1999).

32. Crown, A., Moraes, I. R. & Wieckowski, A. Examination of Pt(111)/Ru and Pt(111)/Os surfaces: STM imaging and methanol oxidation activity. *J. Electroanal. Chem.* **500**, 333–343 (2001).

33. Over, H. *et al.* Atomic-Scale Structure and Catalytic Reactivity of the RuO_2 (110) Surface. *Science* **287**, 1474–1476 (2000).

34. Cong, N. *et al.* Nanoporous RuO2 characterized by RuO(OH)2 surface phase as an efficient bifunctional catalyst for overall water splitting in alkaline solution. *J. Electroanal. Chem.* **881**, 114955 (2021).

35. Böttcher, A., Niehus, H., Schwegmann, S., Over, H. & Ertl, G. CO Oxidation Reaction over Oxygen-Rich Ru(0001) Surfaces. *J. Phys. Chem. B* **101**, 11185–11191 (1997).

36. Over, H. *et al.* Visualization of Atomic Processes on Ruthenium Dioxide using Scanning Tunneling Microscopy. *ChemPhysChem* **5**, 167–174 (2004).

37. Einstein, A. Über einen die Erzeugung und Verwandlung des Lichtes betreffenden heuristischen Gesichtspunkt. *Ann. Phys.* **322**, 132–148 (1905).

38. *Handbook of X-ray photoelectron spectroscopy: a reference book of standard spectra for identification and interpretation of XPS data*. (Perkin-Elmer Corporation, 1992).

39. Hofmann, S. *Auger- and X-Ray Photoelectron Spectroscopy in Materials Science*. vol. 49 (Springer Berlin Heidelberg, 2013).

40. Powell, C. J., Jablonski, A., Tanuma, S. & Penn, D. R. Effects of elastic and inelastic electron scattering on quantitative surface analyses by AES and XPS. *J. Electron Spectrosc. Relat. Phenom.* **68**, 605–616 (1994).

41. Tersoff, J. & Hamann, D. R. Theory of the scanning tunneling microscope. *Phys. Rev. B* **31**, 805–813 (1985).

42. Jonat, F. & Jr, J. A. S. Low-energy electron diffraction for surface structure analysis. 60.

43. Povar, I. & Spinu, O. Ruthenium redox equilibria: 3. Pourbaix diagrams for the systems Ru-H2O and Ru-Cl--H2O. 10 (2016).

44. Berg, M. *et al.* Atomic step disorder on polycrystalline surfaces leads to spatially inhomogeneous work functions. *J. Vac. Sci. Technol. A* **40**, 023207 (2022).

45. Gallego, S., Ocal, C. & Soria, F. Surface and bulk reconstruction of Pt(111) 1 × 1. *Surf. Sci.* **377–379**, 18–22 (1997).

46. Lu, C. *et al.* UHV, Electrochemical NMR, and Electrochemical Studies of Platinum/Ruthenium Fuel Cell Catalysts. *J. Phys. Chem. B* **106**, 9581–9589 (2002).

47. Lu, C. & Masel, R. I. The Effect of Ruthenium on the Binding of CO, H_2, and H_2O on Pt(110). *J. Phys. Chem. B* **105**, 9793–9797 (2001).

48. Chandra, D., Garner, M. L. & Lau, K. H. Vapor pressures of osmium, rhodium, and ruthenium carbonyls. *J. Phase Equilibria* **20**, 565–572 (1999).

49. Galhenage, R. P. *et al.* Platinum–ruthenium bimetallic clusters on graphite: a comparison of vapor deposition and electroless deposition methods. *Phys. Chem. Chem. Phys.* **17**, 28354–28363 (2015).

50. Maier, S., Stass, I., Cerdá, J. I. & Salmeron, M. Unveiling the Mechanism of Water Partial Dissociation on Ru(0001). *Phys. Rev. Lett.* **112**, 126101 (2014).

51. Morgan, D. J. Resolving ruthenium: XPS studies of common ruthenium materials. *Surf. Interface Anal.* **47**, 1072–1079 (2015).

52. Shelberg, M., Lam, N. & Moellering, H. Measuring the Fractal Dimensions of Surfaces. 11 (1983).

53. Gómez-Rodríguez, J. M., Asenjo, A., Salvarezza, R. C. & Baró, A. M. Measuring the fractal dimension with STM: application

to vacuum-evaporated gold. *Ultramicroscopy* **42–44**, 1321–1328 (1992).

54. Dobrescu, G. *et al.* Modified Catalysts and Their Fractal Properties. *Catalysts* **11**, 1518 (2021).
55. Tu, Y. *et al.* Double-layer hybrid chainmail catalyst for high-performance hydrogen evolution. *Nano Energy* **72**, 104700 (2020).
56. Yu, L., Deng, D. & Bao, X. Chain Mail for Catalysts. *Angew. Chem.* **132**, 15406–15409 (2020).